# Gold remobilisation and formation of high grade ore shoots driven by dissolution-reprecipitation replacement and Ni substitution into auriferous arsenopyrite

Denis Fougerouse[1]*, Steven Micklethwaite[1,2], Andrew G. Tomkins[2], Yuan Mei[2,3], Matt Kilburn[4], Paul Guagliardo[4], Louise A. Fisher[5], Angela Halfpenny[5,6], Mary Gee[1], David Paterson[7], Daryl L. Howard[7]

[1]Centre for Exploration Targeting, The University of Western Australia, Crawley, WA, Australia
[2]School of Earth, Atmosphere & Environment, Monash University, Melbourne, Victoria, Australia
[3]CSIRO Mineral Resources Flagship, Clayton, Victoria, Australia
[4]Centre for Microscopy, Characterisation and Analysis, The University of Western Australia, 35 Stirling Highway, Crawley, WA 6009, Australia
[5]CSIRO Mineral Resources Flagship, Bentley, Western Australia, Australia
[6]Microscopy & Microanalysis Facility, John de Later Centre, Curtin University, Perth, Western Australia, Australia
[7]XFM Beamline, Australian Synchrotron, Clayton, Victoria, Australia

*Corresponding author: denis.fougerouse@research.uwa.edu.au

**Abstract**

Both gold-rich sulphides and ultra-high grade native gold oreshoots are common but poorly understood phenomenon in orogenic-type mineral systems, partly because fluids in these systems are considered to have relatively low gold solubilities and are unlikely to generate high gold concentrations. The world-class Obuasi gold deposit, Ghana, has gold-rich arsenopyrite spatially associated with quartz veins, which have extremely high, localised concentrations of native gold, contained in microcrack networks within the quartz veins where they are folded. Here, we examine selected samples from Obuasi using a novel combination of quantitative electron backscatter diffraction analysis, ion microprobe imaging, synchrotron XFM mapping and geochemical modelling to investigate the origin of the unusually high gold concentrations. The auriferous arsenopyrites are shown to have undergone partial replacement (~15%) by Au-poor, nickeliferous arsenopyrite, during localised crystal-plastic deformation, intragranular microfracture and metamorphism (340°-460°C, 2 kbars). Our results show the dominant replacement mechanism was pseudomorphic dissolution-reprecipitation, driven by small volumes of an infiltrating fluid that had relatively low $fS_2$ and carried aqueous $NiCl_2$. We find that arsenopyrite replacement produced strong chemical gradients at crystal-fluid interfaces due to an increase in $fS_2$ during reaction, which enabled efficient removal of gold to the fluid phase and development of anomalously gold-rich fluid (potentially 10ppm or more depending on sulphur concentration). This process was facilitated by precipitation of ankerite, which removed $CO_2$ from the fluid, increasing the relative proportion of sulphur for gold complexation and inhibited additional quartz precipitation. Gold re-precipitation occurred over distances of 10 µm to several tens of meters and was likely a result of sulphur activity reduction through precipitation of pyrite and other sulphides. We suggest this late remobilisation process may be relatively common in orogenic belts containing abundant mafic/ultramafic rocks, which act as a source of Ni and Co scavenged by chloride-bearing fluids. Both the preference of the arsenopyrite crystal structure for Ni and Co, rather than gold, and the release of sulphur during reaction, can drive gold remobilisation in many deposits across broad regions.

## 1. Introduction

Trace element remobilisation occurs when an element contained in a primary mineral is released from the crystal structure, allowing it to be transported to new locations, often at high concentrations, a short distance away (millimetres to hundreds of metres; Marshall et al. 2000). This type of remobilisation is particularly relevant to understanding the distribution of precious metals in deformed and metamorphosed ore deposits. But our understanding of how trace elements are remobilised is also critical to a wide range of environments, including gold transport in the regolith profile of weathered terrains (Hough et al., 2007), mobility of deleterious metals in soils (Chuan et al., 1996; Kalbitz and Wennrich, 1998) and potentially disturbed geochronological isotope systems in zircons and monazites

(Geisler et al., 2007; Harlov et al., 2011; Reddy et al., 2006). However, when it comes to precious metal remobilisation under mid-crustal conditions the process is controversial due to the inferred low solubilities of these elements in aqueous fluids, the extremely slow rates of element diffusion in minerals and poor understanding of how metals are soluble in one location but re-precipitated just a short distance away. Despite these arguments, there is a common spatial relationship between primary sulphides containing trace metals in their crystal structure, and nearby, texturally younger concentrations of those metals, often at very high grades (Cook et al., 2009; Cook et al., 2013; Dubé et al., 2004; Fougerouse et al., in press; Large et al., 2007; Morey et al., 2008).

Metal migration has been documented in volcanic massive sulphides (VMS) systems (Cook et al., 1998; Cook, 1996; Le Vaillant et al., 2015; Marshall and Gilligan, 1993; Tomkins, 2007), iron ore systems (Angerer et al., 2013; Duuring and Hagemann, 2013) and also in gold systems (Cook et al., 2009; Cook et al., 2013; Dubé et al., 2004; Morey et al., 2008; Tomkins and Mavrogenes, 2002; Tomkins et al., 2004). Although some of the mechanisms involved in this remobilisation are not understood, it led to the migration of Ni up to 250 m away from the primary mineralisation of the Miitel Ni sulphide deposit (Le Vaillant et al., 2015), the significant upgrade of hypogene ores at the Beebyn iron deposit (Duuring and Hagemann, 2013) and spectacular native gold occurrences in the Red Lake gold deposit (Dubé et al., 2004).

In this study we investigate the well-documented Obuasi gold deposit, Ghana (Allibone et al., 2002; Fougerouse et al., in press; Oberthür et al., 1994), which provides a natural laboratory to address the issue of remobilisation, due to the presence of very high concentrations of native gold in the hinges of folded quartz veins and a spatial association with gold-rich arsenopyrite in metasedimentary wall rocks. We combine state-of-the-art analytical methods (X-ray fluorescence synchrotron mapping, high resolution secondary ion mass spectrometry, electron backscattered diffraction and scanning electron microscopy) to examine the distribution of gold across multiple scales and identify the mechanisms that may have contributed to the loss of gold from arsenopyrite and its reprecipitation in native form.

## 2. Previous studies on trace element remobilisation

At the mineral scale, three mechanisms are linked to trace element mobility; (1) fluid-mediated replacement; (2) intragrain diffusion and; (3) partial melting of the sulphide ore. The partial melting of sulphide ores has been interpreted to occur in high grade metamorphic mineral deposits (Bailie and Reid, 2005; Frost et al., 2002; Mavrogenes et al., 2001; Sparks and Mavrogenes, 2005; Tomkins et al., 2007; Tomkins et al., 2004), but also at greenschist facies conditions and low temperatures (Biagioni et al., 2013; Ciobanu et al., 2006). This process is possible due to the presence of low-melting-point chalcophile elements (LMCE), which significantly lower the melting temperature of the sulphides. These low temperature melts have the capability to scavenge metals with high melting points such as gold (Ciobanu et al., 2006; Tooth et al., 2008; Tooth et al., 2011), potentially allowing a zone refining

process to persist long after formation of the primary deposit (Cockerton and Tomkins, 2012). The melt usually crystallises as multi-mineral clusters of sulfosalts, tellurides, sulphides and native metals, with curvilinear boundaries and droplet-shaped minerals (e.g., Voudouris et al. 2013). In the system Fe–As–S, the first melt can appear at temperatures as low as 281°C (Frost et al., 2002), but only at S fugacity (*f*S) conditions above the stability of arsenopyrite (see Tomkins et al., 2004).

Intragrain diffusion is potentially important for trace element remobilisation and operates via a broad range of sub-mechanisms, the three most important being volume diffusion, high diffusivity pathway diffusion and dislocation–impurity pair (DIP) diffusion (Klinger and Rabkin, 1999; Plümper et al., 2012; Reddy et al., 2007; Timms et al., 2011; Vukmanovic et al., 2014). In the diffusion model, the migration of large atomic radii elements such as gold is best explained by high diffusivity pathway and DIP diffusions sub-mechanisms (Plümper et al., 2012; Reddy et al., 2006; Vukmanovic et al., 2014), whereas the volume diffusion mechanism is usually regarded as being too slow to be effective at mid-crustal temperatures (~300-450 °C). As a result of the migration of dislocations and elements in minerals, primary internal crystallographic zonation is usually at least partially erased and becomes diffuse or non-existent, whereas major element compositions remain unchanged. The operation of these diffusion mechanisms have been interpreted to explain rare earth element redistribution in zircons (Reddy et al., 2006; Valley et al., 2014) and trace element compositional variation and phase exsolution in sulphides hosted in mineral deposits (Reddy and Hough, 2013; Tomkins and Mavrogenes, 2001; Vukmanovic et al., 2014).

Fluid-mediated replacement reactions, or coupled dissolution-reprecipitation reactions (Putnis, 2009), are potentially an extremely effective mechanism for major and trace element modifications in minerals (Geisler et al., 2007; Harlov et al., 2011; Xia et al., 2009; Zhao et al., 2009). This reaction occurs when elements introduced by a fluid cause a mineral phase to be replaced either by a new composition of the same phase or by an entirely new phase (Harlov et al., 2011). In the case of one phase being replaced by a new composition of the same phase, the solid solution composition (i.e. non-stoichiometric) of the parent phase has higher solubility in the fluid than the pure stoichiometric end-member of the daughter phase (Geisler et al., 2007; Lippmann, 1980). Trace elements within the parent phase can be stripped out during the reaction and released into the fluid (Martin et al., 2008). Once initiated, the reaction is self-perpetuating (Harlov et al., 2011). The reaction front is sharp, planar to curvilinear and associated with a thin layer of supersaturated fluid film during reaction. The daughter phase can be characterised by interconnected nano- and micro-porosity allowing fluid infiltration to and from the reaction front (Putnis, 2009). In some examples, at advanced stages of the reaction, the interconnected nano- and micro-porosity is not preserved due to complete recrystallisation of the daughter phase and sealing of the porosity (Harlov et al., 2011). In the system under discussion here, gold micronuggets have been observed at many locations where arsenopyrite replaces löllingite, particularly along the reaction front (Neumayr et al., 1993; Tomkins and Mavrogenes, 2001).

## 3. Sample suite and microanalytical methods

### *3.1. Sample suite*

Samples were selected from the Obuasi gold deposit (Ghana). Obuasi is the largest gold deposit discovered in West Africa with about 62 Moz of gold (past production + resources). The host rocks and geological context of the Obuasi deposit are well-documented (Allibone et al., 2002; Fougerouse et al., in press; Oberthür et al., 1994; Yao and Robb, 2000) and shown in Figure 1. The deposit is hosted in the Paleoproterozoic Birimian Kumasi volcanosedimentary basin composed of carbonaceous phyllites, slates, psammites, and volcano-sedimentary rocks (Adadey et al., 2009; Oberthür et al., 1998; Perrouty et al., 2012). The metamorphic conditions were calculated from the mineral assemblage actinolite + chlorite + clinozoisite + quartz + calcite, to have been 340° - 460° and 2 kbar (Schwartz et al., 1992). Over 200 samples were collected from outcropping and underground mineralised exposures throughout the Obuasi mine in order to provide a representative suite of samples for petrographical and geochemical analyses. The main host for the sulphide ores are phyllites composed of micas, quartz, carbonates (ankerite and siderite), chlorites, rutile and graphite.

Two economic styles of mineralisation coexist in the same ore zone; gold-bearing arsenopyrite disseminated in the metasedimentary rocks and native gold in dense fracture networks developed in the hinges of folded quartz veins (Blenkinsop et al., 1994; Fougerouse et al., in press; Oberthür et al., 1994). Arsenopyrite is the dominant ore mineral (60-95%) but pyrite can also be present (Oberthür et al., 1994). Concentrations of gold in the crystal lattice of the arsenopyrites range from 300 to 3000 ppm (Fisher et al., 2014; Fougerouse et al., in press), whereas gold content only reaches 3.3 ppm in pyrite (Oberthür et al., 1994). Although the two styles of mineralisation are spatially associated with one another, they formed during distinct structural events (Fougerouse et al., in press), with gold-bearing arsenopyrite crystallising during early $D2_{Ob}$ whereas the native gold precipitated during $D3_{Ob}$.

Evidence for the timing of arsenopyrite mineralisation includes (Fougerouse et al., in press) quartz-ankerite strain shadows around the arsenopyrites that are parallel with a pervasive $S2_{Ob}$ fabric but refolded by a $S3_{Ob}$ crenulation cleavage. Evidence for the timing of native gold mineralisation in adjacent quartz veins includes (Fougerouse et al., in press) the distribution of the gold in fracture networks in $F3_{Ob}$ fold hinges of the quartz veins, which are semiparallel with the $S3_{Ob}$ crenulation cleavage. Notwithstanding these observations, both styles of mineralisation likely formed within a short time of one another during the Eburnean orogeny, which affected the West African Craton from 2125 to 1980 Ma (Perrouty et al., 2012).

### 3.2. *Analytical methods*

We used a diverse combination of microanalytical techniques to investigate the elemental distribution of trace elements (particularly Au) in the gold-bearing arsenopyrites and their relationship with microstructures formed during crystal-plasticity.

X-ray fluorescence (XRF) mapping provided quantitative multi-element images with their full petrographic context. The application of the method to ore mineral studies is well documented in Fisher et al. (2014). The analyses were performed on the XFM beamline at the Australian Synchrotron (Paterson et al., 2011) using the Maia 384 large angle detector array (Fisher et al., 2014; Kirkham et al., 2010; Ryan et al., 2010a; Ryan et al., 2014). The samples were mapped with a pixel size of 2 μm and dwell time of 7.8125 ms, over areas of a few square millimetres, to permit measurement of trace element concentrations with good counting statistics. Samples were prepared as polished thin sections (30 μm thick) mounted on 1 mm-thick quartz glass slides to minimise arsenic background from the glass slide (Fisher et al., 2014). Standard foils (Mn, Fe, Pt and YF3) were analysed daily to calculate the X-ray flux and monitor drift. The Maia XFM full spectral data were analysed using the GeoPIXE software suite. GeoPIXE applies a fundamental parameters approach, with spectral deconvolution and imaging, using the dynamic analysis method (Ryan, 2000; Ryan et al., 2010b) based on fitting a representative total spectrum and a detailed model of Maia detector array efficiency (Ryan et al., 2010a). The Maia detector has a resolution of 400eV which allows gold peaks to be distinguished in the spectra despite the peak overlap with arsenic (Fisher et al., 2014).

Elemental mapping was carried out using the Cameca NanoSIMS 50 at the Centre for Microscopy, Characterisation and Analysis (CMCA) at The University of Western Australia. The samples were prepared as polished one inch resin mounts and thin sections, and carbon coated to provide conductivity. Measurements were performed with a $Cs^+$ primary beam, with a spot size of approximately 100 nm, impact energy of 16 keV, and a beam current of 2 pA. The instrument was operated in multicollector mode, allowing the simultaneous detection of five ion species ($^{34}S$, $^{54}Fe^{32}S$, $^{60}Ni^{32}S$, $^{75}As^{32}S$ and $^{197}Au$) from the same analysis region. Secondary ion images were obtained by rastering the primary ion beam across areas measuring 100 x 100 μm, at a resolution of 1024 x 1024 pixels (each pixel measuring approximately 97 nm), with dwell times of 21-40 ms per pixel. Prior to imaging, the sample surface was presputtered with the primary ion beam (using 250 pA beam current) to > 2 x $10^{17}$ ions/$cm^2$, in order to remove surface contamination and implant $Cs^+$ ions to reach a steady-state of ion emission.

Mineral identification, mineral chemistry zonation, overprinting relationships and paragenesis were investigated with optical techniques and scanning electron microscopy (SEM). Backscattered electron images were generated using a TESCAN VEGA3 SEM. Energy Dispersive X-ray spectra (EDX) were acquired using an Oxford instruments X-Max 50 silicon drift detector with AZtec software fitted on the TESCAN VEGA3. Analytical conditions were 15 kV accelerating voltage with a 1.5 nA probe current.

Electron backscatter diffraction (EBSD) and EDS data were collected on 1 inch round polished block at the CSIRO Earth Science and Resource Engineering in Kensington (Australia) using a Bruker e-flash detector for EBSD and a Bruker XFlash 5030 silicon drift detector for EDS, all fitted on a Zeiss Ultraplus FEG SEM. The instrument was operated at 20 kV accelerating voltage, 12.10 nA beam current and a tilting angle of 70°. EBSD colours maps show the full crystal orientation, from the centre of each grain.

## 4. Descriptive properties of arsenopyrites, mineral assemblages and native gold distribution

Maia XRF maps, of sample 215-7b are presented in Figures 3 and 5. The matrix is composed of quartz, muscovite, chlorite, ankerite and siderite. The sulphides form aggregates of partially-fragmented arsenopyrite grains and small pyrites. High resolution NanoSIMS elemental maps of areas up to 100x100 $\mu m^2$ allowed investigation of the fine textures of the trace element distribution and the contact between the different domains of the arsenopyrites and microfractures (Figs. 3, 4 and 6).

### *4.1. Arsenopyrite overgrowths and rims*

Mineralised arsenopyrites are generally idiomorphic, acicular and range from 50 µm up to several mm in size. Gold-bearing arsenopyrite is the major component of the disseminated sulphide ores (60-95% - Fig. 1) with lesser pyrite, pyrrhotite, marcasite, and chalcopyrite. The sulphide mineralisation is surrounded by a 50m wide ankerite and siderite alteration halo and the arsenopyrites are commonly surrounded by quartz-ankerite strain shadows developed during $D2_{Ob}$ (Fougerouse et al., in press). The smaller grains are usually homogenous (inclusion-free) under optical microscope, whereas the bigger grains are typically composed of several domains detailed below. The arsenopyrite also contains microfractures and interstitial spaces between grains, filled with ankerite, pyrite and small gold particles, which are interpreted to form during $D3_{Ob}$ (as discussed in section 5).

### *4.2. Crystallographically controlled microtextures and chemistry*

The arsenopyrite grains are composed of at least two primary domains: rims that appear homogenous in BSE images and inclusion-rich cores (Oberthür et al., 1994; Oberthür et al., 1997). The cores contain inclusions of pyrrhotite, chalcopyrite and rutile. The boundary between cores and rims can be rich in silicate inclusions (Figs. 1 and 2). In this study, the combination of the core-and-rim domains are abbreviated as $Apy_{(I)}$. The composition of $Apy_{(I)}$ is non-stoichiometric, being depleted in As (~44 wt% As – table 1). The distribution of the gold in $Apy_{(I)}$ is zoned (Fig. 3), with gold-poor cores and gold-rich rims (300 to 3000 ppm Au in the rims; Fougerouse et al. in press; Fisher et al. 2014).

In the $Apy_{(I)}$ rims, high-resolution NanoSIMS mapping reveals that Au is distributed in alternating, submicron-scale concentric bands (up to 100) with sharp boundaries, despite the homogenous appearance of the $Apy_{(I)}$ in BSE imagery. Gold is the only compositional variation between the bands and no other major or trace element chemistry changes were observed. The bands are concentric and parallel with the euhedral morphology of the grain boundary of the arsenopyrite (Figs. 3, 4 and 6). Each band is typically less than a μm wide, with variable gold content relative to one another and a semi-regular spacing. No micronuggets of native gold were detected in the arsenopyrite grains at the highest resolution of our analysis (100 nm), except in association with microfractures.

Commonly, a third arsenopyrite domain cuts across the mineralised grains, penetrating in from microfractures and grain boundaries. These domains, labelled $Apy_{(II)}$, are characterised by higher As and lower S concentrations, with compositions that are close to stochiometric (~46 wt% As – table 1). $Apy_{(II)}$ domains are nickeliferous and gold-poor. Critically, these gold-poor domains preserve the original shape of the arsenopyrite grains and the contacts between $Apy_{(II)}$ and $Apy_{(I)}$ are sharp, ranging, in the same grains, from planar to curvilinear (Fig. 2). NanoSIMS imaging also demonstrates that the Ni distribution is zoned in the $Apy_{(II)}$ in irregular shaped bands subparallel with the contact between $Apy_{(I)}$ and $Apy_{(II)}$ (Figs. 3 and 6). However, EBSD analysis demonstrates that there are no differences in crystallographic lattice orientation associated with the change between $Apy_{(I)}$ and $Apy_{(II)}$ (Fig. 4) and therefore the crystal orientation did not affected the chemical composition of individual grains.

The EBSD data also show that both high-angle and low-angle boundaries are present in localised domains consistent with crystal-plastic deformation and limited arsenopyrite recrystallisation. In the example presented here (sample 215-20), a high density of crystallographic misorientations are localised in a narrow domain corresponding to the presence of $Apy_{(II)}$, adjacent to a large microfracture filled with pyrite (Fig. 4). In this recrystallised domain, the $Apy_{(II)}$ is up to three times more than in undeformed regions associated with $Apy_{(II)}$ (Fig. 4). These observations suggest a link between crystal-plastic deformation within the arsenopyrite and loss of gold.

### *4.3. Mineral-filled microfractures*

The mineral-filled microfractures can be subdivided into two categories; (1) intragranular microfractures in arsenopyrites and (2) microfracture networks in folded quartz veins. The intragranular arsenopyrite microfractures can develop from grain boundaries and terminate within the arsenopyrite or entirely dissect the grains. They are usually filled with xenomorphic pyrite and chlorite, but also with native gold particles up to 10 μm. Ankerite and quartz are not present. Importantly, $Apy_{(II)}$ forms semi-symmetric halos around the intragranular arsenopyrite microfractures. The pyrite within the intragranular microfractures has fine-scale Ni zoning and is usually Au-poor but contains native gold inclusions (Figs. 3, 5 and 6). Such Ni-enriched pyrite is referred to here as $Py_{(III)}$. The $Py_{(III)}$ is also

developed in the intergranular regions between arsenopyrite grains and is in textural equilibrium with interstitial ankerite (Figs. 3 and 5).

Figure 6 shows an example of an intragranular microfracture cutting through an $Apy_{(I)}$ grain, including its gold-rich epitaxial zonation. This microfracture is infilled with $Py_{(III)}$ and bordered by a rim of $Apy_{(II)}$ before sharply transitioning to $Apy_{(I)}$. Au and Ni concentrations measured in a traverse from the microfracture to the centre of the grain (Fig. 6) confirm that the microfracture is filled with native gold grains and nickeliferous $Py_{(III)}$. The Au concentrations in the $Apy_{(II)}$ are below detection limit (XRF synchrotron; 400 ppm for this analysis), while the $Apy_{(I)}$ has gold concentrations up to 2000 ppm. In the $Apy_{(II)}$, close to the contact with the $Apy_{(I)}$, the Ni concentrations attain maximum values of 2880 ppm.

The microfracture networks in the quartz veins (microfractures type 2) can be observed in hand specimen and are usually radiating from larger fractures parallel with the $S3_{Ob}$ cleavage. They are particularly well developed in the hinges of the $F3_{Ob}$ folds. Large native gold particles are exclusively hosted in the quartz microfractures, which was demonstrated using 3D mapping of gold distribution in a mineralised quartz sample by high-resolution X-ray computed tomography (Fougerouse et al., in press). Typically, these gold particles are several hundreds of micrometres across and up to several centimetres long. A polymetallic suite of accessory minerals is solely associated with the microfractures in the quartz veins and is not found in the wall rocks. These accessory minerals include galena, chalcopyrite, sphalerite, bournonite, boulangerite, tetrahedrite, aurostibine, löllingite, pyrite, arsenopyrite, and rare bismuth tellurides (Oberthür et al., 1994). Muscovites and chlorites also infill the microfractures. They are vein selvages derived from wall rock fragments (Fig. 1D).

## 5. Discussion

### *5.1. Interpretation of mineral textures timing relationships and mass balance estimates*

From the overprinting textural relationships a clear sequence of events with respect to gold can be determined at the mineral scale. (1) The fine oscillatory zoning within $Apy_{(I)}$, defined by gold concentration (Fig. 3D and E), developed first. This is interpreted to reflect crystallographic, growth-rate-controlled incorporation into the crystal lattice of primary arsenopyrite developed during an initial hydrothermal event (Barker and Cox, 2011; Barker et al., 2009; Chouinard et al., 2005), rather than variations in fluid composition deriving from multiple separate hydrothermal events, which would have also led to major chemistry changes between different bands (Barker et al., 2009). (2) $Apy_{(II)}$ cuts across the epitaxial zones of $Apy_{(I)}$ and therefore postdates $Apy_{(I)}$ (Fig. 2A-C). This nickeliferous $Apy_{(II)}$ is spatially associated and coeval with Ni-bearing $Py_{(III)}$ and native gold located in the intragranular arsenopyrite microfractures. $Py_{(III)}$ is also intergrown, and therefore in textural equilibrium, with late-stage ankerite that fills fractures and spaces between Apy grains (Fig. 3A). (4) Because the dimensions

of $Apy_{(II)}$ are enhanced by the presence of sub-grains and intragranular microfractures formed during $D3_{Ob}$, it is interpreted that $Apy_{(II)}$, $Py_{(III)}$, native gold and the interstitial ankerite developed at the later stages of the $D3_{Ob}$ deformation event. A second generation of chlorite overgrew the $S3_{Ob}$ cleavage and would have also formed during this late gold event (Fougerouse et al., in press). Quartz is notably absent from the microfracture networks that host remobilised gold, suggesting that silica was undersaturated in the fluid phase.

The quantity of gold remobilised from individual arsenopyrite grains was estimated using 2D surface area calculations. In individual images, the surface area of the $Apy_{(II)}$ was measured (average of 15% of the total grain surface) and the quantity of gold removed was calculated based on an average concentration for $Apy_{(I)}$ of 1000 ppm (Fisher et al., 2014; Fougerouse et al., in press). The surface areas of the native gold particles were similarly measured and the quantity of gold estimated based on the assumption that they are 100% gold (i.e., a maximum estimate). It was found the native gold in fractures amongst arsenopyrite represents only 30-70 % of the gold extracted from the arsenopyrites. Therefore, on average 750 ppb of gold was extracted from arsenopyrite per tonne of rock, with between 525 and 225 ppb of Au migrating out of the thin section at distances greater than the thin-section scale (4 cm).

### *5.2. Gold remobilisation from arsenopyrite grains*

A number of characteristics enable us to distinguish the mechanism responsible for gold mobilisation from arsenopyrite. Firstly, the $Apy_{(I)}$ morphology and its crystal lattice orientation are preserved across $Apy_{(I)}$–$Apy_{(II)}$ boundaries even though there is a compositional difference between the two arsenopyrite types, with $Apy_{(II)}$ containing lower S and higher As content. Secondly, native gold in the intragranular microcracks within arsenopyrite is neither associated with clusters of sulfosalts, tellurides, sulphides and native metals, nor curvilinear boundaries. Finally, the boundary between $Apy_{(I)}$ and $Apy_{(II)}$ is sharp, suggesting intragrain diffusion was not the predominant mechanism for gold remobilisation.

Given that gold can be mobile in a polymetallic melt at temperatures well below 340°C (Cockerton and Tomkins, 2012; Oberthür and Weiser, 2008; Tomkins et al., 2004), and that the metamorphic peak reached 340 - 460°C, we will briefly consider the possibility that some gold was mobilised as a liquid. In the system Fe–As–S, the first melt can appear at temperatures as low as 281°C (Frost et al., 2002), but only when the sulfur fugacity is high and beyond the arsenopyrite stability field (Tomkins et al., 2004), which is clearly not the case at Obuasi. The polymineralic accumulations containing gold in the quartz veins (Fig. 1F) are reminiscent of the textures formed by crystallisation of gold-bearing polymetallic liquids, but the phase relations in the relevant system (Au-Sb-As-Pb-Cu-Fe-S) suggest that the assemblage would have been solid at the peak metamorphic conditions (see Tomkins et al., 2004). At these temperatures and $fS_2$ conditions necessary to stabilise arsenopyrite, the system would need to contain native bismuth or mercury at low $fS_2$, or thallium as part of the sulfosalt assemblage (cf. Tooth

et al., 2008; Tomkins et al., 2004); however, such phases are not present. Therefore, we find that at Obuasi, it is unlikely that a gold-rich polymetallic melt ever developed.

Instead, our evidence indicates the dominant mechanism was pseudomorphic replacement of arsenopyrite by fluid-mediated dissolution-reprecipitation (Borg et al., 2014; Corfu et al., 2003; Geisler et al., 2007; Harlov et al., 2005; Putnis, 2009). In this case the relevant reaction is:

$$Au_xFe_{1-x}AsS_{high\ S} + yNiCl_{2(aq)} + 2H_2O_{(aq)} + e^- \rightarrow Ni_yFe_{1-y}AsS_{low\ S} + xAu(HS)_2^-{}_{(aq)} + 2y\ HCl_{(aq)} + O_2 \quad [1]$$

Where "x" and "y" are much less than 1 and represent the trace element concentration of Au and Ni, respectively. Geochemical modelling generated using Geochemist's Workbench software (Bethke, 2008) and thermodynamic properties from the HCh database (Shvarov, 2008; Shvarov and Bastrakov, 1999) supports this interpretation and enables us to constrain the fluid chemistry. Figure 7 shows the activity diagram for the predominant speciation of Au and Ni at 350 ºC, 2 kbar as a function of pH and oxygen fugacity. As shown in Figure 7, the concentration of Au in solution can reach anomalous values, up to 10 ppm at pH = 6 to 7 and log$fO_2$ = -32 to -28, near the pH of $HS^-/H_2S$ equivalence point and the pyrite-pyrrhotite redox buffer, which is 1-3 orders of magnitude more than expected for orogenic systems (Mikucki, 1998) and 3 orders of magnitude more than measured in deep, gold-rich geothermal fluids (Simmons and Brown, 2007). At the same pH and redox conditions, Ni is predominantly stable as a solid sulphide mineral phase (Fig. 7). The loss of sulphur associated with Ni replacement of Fe in arsenopyrite (Table 1) is critical because it increases the solubility of gold as a $Au(HS)_2^-$ complex (Liu et al., 2014) at the crystal-fluid interface, promoting liberation of gold from the solid phase and remobilisation. The reaction model also shows that at increasing $fS_2$, Ni precipitates whereas Au dissolves in the solution (Fig. 8). This may be coupled with the apparent tendency of Ni to inhibit accommodation of gold in the arsenopyrite structure (i.e., based on our observations), which if true, would also promote remobilisation. Such a possibility can be addressed by considering how Au and Ni are substituted into the arsenopyrite structure. Along with a proportion of nanoparticulate gold, it is thought that $Au^+$ substitutes to a small extent (a few thousand ppm) for six-fold coordinated $Fe^{3+}$ in arsenopyrite (see summary of previous work in (Cabri et al., 2000), although there may be some non-systematic incorporation into lattice defects (Reich et al., 2005). It should be noted that the nature of gold substitution in arsenopyrite is still not well understood and XAS and x-ray crystallography studies indicate that the bonding environment of gold in arsenopyrite is complex. In contrast, there is complete solid solution between FeAsS and NiAsS (gersdorffite), as well as CoAsS (cobaltite). The ionic radii of six-fold coordinated $Fe^{3+}$ and $Ni^{3+}$ are 0.785 and 0.74 Å respectively ($Co^{3+}$ is 0.75 Å), whereas that of $Au^+$ is 1.51 Å (Shannon, 1976), so Au does not fit as easily into the arsenopyrite structure as Ni. Similarly, the difference in ionic charge of Au to that of Ni (and Co) relative to Fe, implies that Ni should be preferentially substituted for Au in arsenopyrite. It should therefore be expected that both Ni and Co would preferentially replace gold in the arsenopyrite crystal structure if they became available

via a later fluid. In regards to gold in lattice defects, it may be that the Ni replacement process heals defect structures, leaving gold more susceptible to fluid complexation.

One of the interesting features of the system studied here is that there was little or no quartz precipitation during remobilisation of the gold into the microfracture networks in quartz, requiring that the fluid was $SiO_2$ undersaturated. Fundamentally, decreasing temperature causes a decrease in $SiO_2$ solubility in $H_2O$, so fluids infiltrating from a hotter source region below should tend to precipitate quartz. Nonetheless, typical orogenic fluids are not pure $H_2O$, and at any given temperature $SiO_2$ solubility varies as a function of $H_2O$ activity. Since quartz is relatively insoluble in $CO_2$ (Newton and Manning, 2000; Shmulovich et al., 2001), quartz solubility will decrease with increasing $XCO_2$. The late fluid responsible for gold remobilisation was likely a typical orogenic $H_2O$–$CO_2$–$H_2S$ fluid that had equilibrated with regional rocks, and thus was quartz-saturated or even supersaturated upon infiltration. However, precipitation of the intergranular ankerite would have removed $CO_2$ from the fluid, necessitating an increase in the solubility of quartz in the fluid, thus inhibiting quartz precipitation and possibly even allowing some quartz dissolution. An additional consequence of this process is that by removing $CO_2$ from the fluid, the relative abundance of $H_2S$ increases thereby further enhancing the solubility of gold and buffering the fluid chemistry towards the ideal pH conditions for gold dissolution.

We calculated the effect of removing $CO_2$ from the Au and Si rich system. As shown in Figure 9A, the solubility of Si has potential to increase from 500 to 3000 ppm during the removal of $CO_2$, especially in the range of 2 – 0 wt% of $CO_2$ in fluids; quartz is rapidly dissolved with a corresponding pH change from 7-8 (Fig. 9B). The solubility of Au increases from 400 to 800 ppm when $CO_2$ content decreases to 5 wt% in the fluids; however, the Au solubility drops to ~20 ppm when $CO_2$ is totally removed. The decrease of Au solubility by about two orders of magnitude corresponds to the change of pH from 6.8 to 8, which is consistent with the activity diagram shown in Figure 7. The pH changes from 5.7 to 8, when removing $CO_2$, crosses the $HS^-/H_2S$ equivalence point, whereas $fO_2$ changes in a very narrow range and stays in the pyrite stability field ($\log fO2 = -30 \sim -28.9$). The total sulphur content in the fluid increases through the reactions and controls the Au carrying ability of the fluid. The preferred pH condition for Au mobility is neutral (6-6.8) whereas Si is more mobile at neutral to alkaline conditions (>6.5). An important conclusion is that moderation of $XCO_2$ through carbonate precipitation can control both Au remobilisation and Si solubility in $H_2O$-$CO_2$ fluid systems.

Two observations indicate that only a low volume of fluid percolated through the metasediments during arsenopyrite replacement and gold remobilisation. Firstly, the primary silicate alteration mineral is chlorite, which overprints $S3_{Ob}$, yet there has been only minor new chlorite formation in the host metasedimentary rocks close to the quartz veins. Secondly, the arsenopyrites have been only sporadically and partially replaced, whereas this process would have been comprehensive if large volumes of fluid had pervaded during $D3_{Ob}$. Given the locally very high concentrations of gold in some fractures, and the low volume of fluid infiltration, the remobilising fluid must have been characterised by very high Au in solution. Such a fluid would be fundamentally different to the large volume and

comparatively dilute fluids usually associated with hydrothermal orogenic gold deposits (McCuaig and Kerrich, 1998; Micklethwaite et al., 2015; Mikucki, 1998). In our model this attainment of unusually high gold solubility conditions was facilitated by three processes that occurred at the sites of pre-existing gold mineralisation: (1) replacement of Au-rich arsenopyrite by Au-free and Ni rich arsenopyrite liberated gold whilst simultaneously increasing the amount of sulphur available for gold complexation at the crystal-fluid interface, (2) precipitation of ankerite removed $CO_2$ from solution, increasing the proportion of sulphur in solution and thus gold solubility, and (3) ankerite precipitation buffered fluid pH towards the ideal conditions for maximising gold solubility, near the $H_2S$–$HS^-$ equivalence point of 6 - 6.8 (Figs. 7, 9).

The subsequent loss of sulphur from the fluid, as pyrite precipitates in the microcracks, acted to lower gold solubility and promote re-precipitation of gold. Such interactions explain why there is an association between gold and pyrite in fractures in arsenopyrite and why remobilisation can occur over short length-scales. Nonetheless, as long as some sulphur remains in the fluid, gold can also be mobilised greater distances. We therefore suggest that the gold found in the microfracture networks in deformed quartz veins was derived from the gold-bearing arsenopyrite, implying remobilisation distances exceeding several tens of meters as the fluids evolved to higher sulphur content through reaction (Fig. 10). The fluid migrated along cleavage planes, grain boundaries and wall rock microfractures to the quartz veins. Folding and fracturing of the quartz veins established an interconnected microfracture network and created a hydraulic gradient, causing fluids to migrate into the microfractures in quartz vein fold hinges where high grade oreshoots ultimately developed (Fig. 10).

### *5.3. Global Implications*

Given that both Ni and Co are transported as chloride species (Liu et al., 2011; Liu et al., 2012; Tian et al., 2012), typical orogenic fluids, which have 3-7 wt.% NaCl equivalent (Ridley and Diamond, 2000), should be capable of providing sufficient quantities of these metals to cause the observed replacement at Obuasi and elsewhere. However, these metals are not evenly distributed in the crust, so the late fluid would need to interact with some mafic or ultramafic material in which these metals are considerably more abundant. These rock types are relatively abundant in Archean and Proterozoic crust, so this process of late remobilisation may be common to many gold deposits. Indeed, gold is found in fractures in arsenopyrite at numerous occurrences around the world (Cook et al., 2013; Essarraj et al., 2001; Morey et al., 2008; Mumin et al., 1994), and in the few cases where trace element concentrations of Ni and Co have been measured, it can be seen that there are late Ni and/or Co rich overgrowths on arsenopyrite and adjacent Au in fractures (e.g., Fig. 6 in Cook et al., 2013; Fig.7 in Morey et al. 2008).

## 6. Conclusions

In the Obuasi gold deposit, interaction between an early generation of gold-bearing arsenopyrite and a later generation of low volume, relatively low $fS_2$ fluid, carrying aqueous $NiCl_2$, initiated replacement reactions in arsenopyrites and liberated gold in solution. During this reaction, liberation of sulphur from the arsenopyrite and precipitation of ankerite increased the solubility of gold and silica significantly, allowing gold to be transported over distances exceeding 50 m. The folding and fracturing of the quartz veins drove the fluid migration into and through the fold hinges of the quartz veins and promoted precipitation of polymetallic sulphides and native gold in the fracture network of the quartz veins.

## Acknowledgments

This study derives from Ph.D. research by Denis Fougerouse. AngloGold Ashanti Ltd is acknowledged for excellent financial support and field assistance. Components of this research were undertaken on the X-ray fluorescence microscopy beamline at the Australian Synchrotron, Victoria, Australia. The data presented in this paper were collected as part of run 6666. The authors acknowledge Dr. Weihua Liu for the discussion of geochemical modelling. The authors also acknowledge the facilities, and the scientific and technical assistance of the Australian Microscopy & Microanalysis Research Facility at the Centre for Microscopy, Characterisation & Analysis, The University of Western Australia, a facility funded by the University, State and Commonwealth Governments. Steven Micklethwaite was funded by the Hammond-Nisbet Endowment.

## References


Adadey, K., Clarke, B., Théveniaut, H., Urien, P., Delor, C., Roig, J. and Feybesse, J. (2009) Geological map explanation-Map sheet 0503 B (1: 100 000), CGS/BRGM/Geoman. Geological Survey Department of Ghana (GSD). No MSSP/2005/GSD/5a.

Allibone, A.H., McCuaig, T.C., Harris, D., Etheridge, M., Munroe, S., Byrne, D., Amanor, J. and Gyapong, W. (2002) Structural Controls on Gold Mineralization at the Ashanti Gold Deposit, Obuasi, Ghana. Society of Economic Geologists Special Publication 9, 29.

Angerer, T., Hagemann, S.G. and Danyushevsky, L. (2013) High-grade iron ore at Windarling, Yilgarn Craton: a product of syn-orogenic deformation, hypogene hydrothermal alteration and supergene modification in an Archean BIF-basalt lithostratigraphy. Mineral. Deposita 48, 697-728.

Bailie, R. and Reid, D. (2005) Ore textures and possible sulphide partial melting at Broken Hill, Aggeneys, South Africa I: petrography. South African Journal of Geology 108, 51-70.

Barker, S.L. and Cox, S.F. (2011) Oscillatory zoning and trace element incorporation in hydrothermal minerals: insights from calcite growth experiments. Geofluids 11, 48-56.

Barker, S.L., Hickey, K.A., Cline, J.S., Dipple, G.M., Kilburn, M.R., Vaughan, J.R. and Longo, A.A. (2009) Uncloaking invisible gold: use of nanoSIMS to evaluate gold, trace elements, and sulfur isotopes in pyrite from Carlin-type gold deposits. Economic Geology 104, 897-904.

Bethke, C.M. (2008) Geochemical and biogeochemical reaction modeling, second ed. Cambridge University Press.

Biagioni, C., D'Orazio, M., Vezzoni, S., Dini, A. and Orlandi, P. (2013) Mobilization of Tl-Hg-As-Sb-(Ag, Cu)-Pb sulfosalt melts during low-grade metamorphism in the Alpi Apuane (Tuscany, Italy). Geology 41, 747-750.

Blenkinsop, T., Schmidt Mumm, A., Kumi, R. and Sangmor, S. (1994) Structural geology of the Ashanti gold mine. Geologisches Jahrbuch D 100, 131-153.

Borg, S., Liu, W., Pearce, M., Cleverley, J. and MacRae, C. (2014) Complex mineral zoning patterns caused by ultra-local equilibrium at reaction interfaces. Geology 42, 415-418.

Cabri, L.J., Newville, M., Gordon, R.A., Crozier, E.D., Sutton, S.R., McMahon, G. and Jiang, D.-T. (2000) Chemical speciation of gold in arsenopyrite. The Canadian Mineralogist 38, 1265-1281.

Chouinard, A., Paquette, J. and Williams-Jones, A.E. (2005) Crystallographic controls on trace-element incorporation in auriferous pyrite from the Pascua epithermal high-sulfidation deposit, Chile–Argentina. The Canadian Mineralogist 43, 951-963.

Chuan, M.C., Shu, G.Y. and Liu, J.C. (1996) Solubility of heavy metals in a contaminated soil: Effects of redox potential and pH. Water Air Soil Pollut 90, 543-556.

Ciobanu, C., Cook, N., Damian, F. and Damian, G. (2006) Gold scavenged by bismuth melts: An example from Alpine shear-remobilizates in the Highiş Massif, Romania. Mineralogy and Petrology 87, 351-384.

Cockerton, A.B. and Tomkins, A.G. (2012) Insights into the Liquid Bismuth Collector Model Through Analysis of the Bi-Au Stormont Skarn Prospect, Northwest Tasmania. Economic Geology 107, 667-682.

Cook, N., Spry, P. and Vokes, F. (1998) Mineralogy and textural relationships among sulphosalts and related minerals in the Bleikvassli Zn-Pb-(Cu) deposit, Nordland, Norway. Mineral. Deposita 34, 35-56.

Cook, N.J. (1996) Mineralogy of the sulphide deposits at Sulitjelma, northern Norway. Ore Geology Reviews 11, 303-338.

Cook, N.J., Ciobanu, C.L. and Mao, J. (2009) Textural control on gold distribution in As-free pyrite from the Dongping, Huangtuliang and Hougou gold deposits, North China Craton (Hebei Province, China). Chemical Geology 264, 101-121.

Cook, N.J., Ciobanu, C.L., Meria, D., Silcock, D. and Wade, B. (2013) Arsenopyrite-pyrite association in an orogenic gold ore: tracing mineralization history from textures and trace elements. Economic Geology 108, 1273-1283.

Corfu, F., Hanchar, J.M., Hoskin, P.W. and Kinny, P. (2003) Atlas of zircon textures. Reviews in Mineralogy and Geochemistry 53, 469-500.

Dubé, B., Williamson, K., Mcnicoll, V., Malo, M., Skulski, T., Twomey, T. and Sanborn-Barrie, M. (2004) Timing of Gold Mineralization at Red Lake, Northwestern Ontario, Canada: New Constraints from U-Pb Geochronology at the Goldcorp High-Grade Zone, Red Lake Mine, and the Madsen Mine. Economic Geology 99, 1611-1641.

Duuring, P. and Hagemann, S. (2013) Leaching of silica bands and concentration of magnetite in Archean BIF by hypogene fluids: Beebyn Fe ore deposit, Yilgarn Craton, Western Australia. Mineral. Deposita 48, 341-370.

Essarraj, S., Boiron, M.-C., Cathelineau, M. and Fourcade, S. (2001) Multistage deformation of Au-quartz veins (Laurieras, French Massif Central): evidence for late gold introduction from microstructural, isotopic and fluid inclusion studies. Tectonophysics 336, 79-99.

Fisher, L.A., Fougerouse, D., Cleverley, J.S., Ryan, C.G., Micklethwaite, S., Halfpenny, A., Hough, R.M., Gee, M., Paterson, D. and Howard, D.L. (2014) Quantified, multi-scale X-ray fluorescence element mapping using the Maia detector array: application to mineral deposit studies. Mineral. Deposita, 1-10.

Fougerouse, D., Micklethwaite, S., Ulrich, S., Miller, J., McCuaig, T.C., Godel, B. and Adams, D. (in press) Evidence for Two Stages of Mineralization in West Africa's Largest Gold Deposit: Obuasi, Ghana. Economic Geology.

523 Frost, B.R., Mavrogenes, J.A. and Tomkins, A.G. (2002) Partial melting of sulfide ore deposits during
524 medium-and high-grade metamorphism. The Canadian Mineralogist 40, 1-18.
525 Geisler, T., Schaltegger, U. and Tomaschek, F. (2007) Re-equilibration of zircon in aqueous fluids and
526 melts. Elements 3, 43-50.
527 Harlov, D.E., Wirth, R. and Förster, H.-J. (2005) An experimental study of dissolution–reprecipitation
528 in fluorapatite: fluid infiltration and the formation of monazite. Contributions to Mineralogy and
529 Petrology 150, 268-286.
530 Harlov, D.E., Wirth, R. and Hetherington, C.J. (2011) Fluid-mediated partial alteration in monazite: the
531 role of coupled dissolution–reprecipitation in element redistribution and mass transfer. Contributions to
532 Mineralogy and Petrology 162, 329-348.
533 Hough, R.M., Butt, C.R.M., Reddy, S.M. and Verrall, M. (2007) Gold nuggets: supergene or hypogene?
534 Australian Journal of Earth Sciences 54, 959-964.
535 Kalbitz, K. and Wennrich, R. (1998) Mobilization of heavy metals and arsenic in polluted wetland soils
536 and its dependence on dissolved organic matter. Science of The Total Environment 209, 27-39.
537 Kirkham, R., Siddons, D., Dunn, P., Kuczewski, A., Dodanwela, R., Moorhead, G., Ryan, C., De
538 Geronimo, G., Beuttenmuller, R. and Pinelli, D. (2010) The Maia spectroscopy detector system:
539 engineering for integrated pulse capture, low-latency scanning and real-time processing, American
540 Institute of Physics Conference Proceedings. Brookhaven National Laboratory (BNL) National
541 Synchrotron Light Source.
542 Klinger, L. and Rabkin, E. (1999) Beyond the fisher model of grain boundary diffusion: Effect of
543 structural inhomogeneity in the bulk. Acta Materialia 47, 725-734.
544 Large, R.R., Maslennikov, V.V., Robert, F., Danyushevsky, L.V. and Chang, Z. (2007) Multistage
545 Sedimentary and Metamorphic Origin of Pyrite and Gold in the Giant Sukhoi Log Deposit, Lena Gold
546 Province, Russia. Economic Geology 102, 1233-1267.
547 Le Vaillant, M., Barnes, S.J., Fiorentini, M.L., Miller, J., McCuaig, T.C. and Muccilli, P. (2015) A
548 Hydrothermal Ni-As-PGE Geochemical Halo Around the Miitel Komatiite-Hosted Nickel Sulfide
549 Deposit, Yilgarn Craton, Western Australia. Economic Geology 110, 505-530.
550 Lippmann, F. (1980) Phase diagrams depicting aqueous solubility of binary mineral systems. Neues
551 Jahrb. Mineral. Abh 139, 1-25.
552 Liu, W., Borg, S.J., Testemale, D., Etschmann, B., Hazemann, J.-L. and Brugger, J. (2011) Speciation
553 and thermodynamic properties for cobalt chloride complexes in hydrothermal fluids at 35–440 C and
554 600bar: an in-situ XAS study. Geochimica et Cosmochimica Acta 75, 1227-1248.
555 Liu, W., Etschmann, B., Testemale, D., Hazemann, J.-L., Rempel, K., Müller, H. and Brugger, J. (2014)
556 Gold transport in hydrothermal fluids: Competition among the Cl−, Br−, HS− and NH 3 (aq) ligands.
557 Chemical Geology 376, 11-19.

Liu, W., Migdisov, A. and Williams-Jones, A. (2012) The stability of aqueous nickel (II) chloride complexes in hydrothermal solutions: Results of UV–Visible spectroscopic experiments. Geochimica et Cosmochimica Acta 94, 276-290.

Marshall, B. and Gilligan, L. (1993) Remobilization, syn-tectonic processes and massive sulphide deposits. Ore Geology Reviews 8, 39-64.

Marshall, B., Vokes, F.M. and Larocque, A.C. (2000) Regional metamorphic remobilization: upgrading and formation of ore deposits.

Martin, L.A., Duchêne, S., Deloule, E. and Vanderhaeghe, O. (2008) Mobility of trace elements and oxygen in zircon during metamorphism: consequences for geochemical tracing. Earth and Planetary Science Letters 267, 161-174.

Mavrogenes, J., MacIntosh, I. and Ellis, D. (2001) Partial melting of the Broken Hill galena-sphalerite ore: Experimental studies in the system PbS-FeS-ZnS-(Ag2S). Economic Geology 96, 205-210.

McCuaig, T.C. and Kerrich, R. (1998) P—T—t—deformation—fluid characteristics of lode gold deposits: evidence from alteration systematics. Ore Geology Reviews 12, 381-453.

Micklethwaite, S., Ford, A., Witt, W. and Sheldon, H. (2015) The where and how of faults, fluids and permeability–insights from fault stepovers, scaling properties and gold mineralisation. Geofluids 15, 240-251.

Mikucki, E.J. (1998) Hydrothermal transport and depositional processes in Archean lode-gold systems: a review. Ore Geology Reviews 13, 307-321.

Morey, A.A., Tomkins, A.G., Bierlein, F.P., Weinberg, R.F. and Davidson, G.J. (2008) Bimodal distribution of gold in pyrite and arsenopyrite: examples from the Archean Boorara and Bardoc shear systems, Yilgarn Craton, Western Australia. Economic Geology 103, 599-614.

Mumin, A.H., Fleet, M.E. and Chryssoulis, S.L. (1994) Gold mineralization in As-rich mesothermal gold ores of the Bogosu-Prestea mining district of the Ashanti Gold Belt, Ghana: remobilization of "invisible" gold. Mineral. Deposita 29, 445-460.

Neumayr, P., Cabri, L.J., Groves, D., Mikucki, E.J. and Jackman, J.A. (1993) The mineralogical distribution of gold and relative timing of gold mineralization in two Archaean settings of high metamorphic grade in Australia. Canadian Mineralogist 31, 711-725.

Newton, R.C. and Manning, C.E. (2000) Quartz solubility in $H_2O$-NaCl and $H_2O$-$CO_2$ solutions at deep crust-upper mantle pressures and temperatures: 2–15 kbar and 500–900 C. Geochimica et Cosmochimica Acta 64, 2993-3005.

Oberthür, T., Vetter, U., Davis, D.W. and Amanor, J.A. (1998) Age constraints on gold mineralization and Paleoproterozoic crustal evolution in the Ashanti belt of southern Ghana. Precambrian Research 89, 129-143.

Oberthür, T., Vetter, U., Schmidt Mumm, A., Weiser, T., Amanor, J., Gyapong, W., Kumi, R. and Blenkinsop, T. (1994) The Ashanti gold mine at Obuasi, Ghana: Mineralogical, geochemical, stable

isotope and fluid inclusion studies on the metallogenesis of the deposit. Geologisches Jahrbuch D 100, 31-129.

Oberthür, T. and Weiser, T. (2008) Gold-bismuth-telluride-sulphide assemblages at the Viceroy Mine, Harare-Bindura-Shamva greenstone belt, Zimbabwe. Mineralogical Magazine 72, 953-970.

Oberthür, T., Weiser, T., Amanor, J.A. and Chryssoulis, S.L. (1997) Mineralogical siting and distribution of gold in quartz veins and sulfide ores of the Ashanti mine and other deposits in the Ashanti belt of Ghana: genetic implications. Mineral. Deposita 32, 2-15.

Paterson, D., De Jonge, M., Howard, D., Lewis, W., McKinlay, J., Starritt, A., Kusel, M., Ryan, C., Kirkham, R. and Moorhead, G. (2011) The X-ray Fluorescence Microscopy Beamline at the Australian Synchrotron, The 10th International Conference On X-Ray microscopy. AIP Publishing, pp. 219-222.

Perrouty, S., Aillères, L., Jessell, M.W., Baratoux, L., Bourassa, Y. and Crawford, B. (2012) Revised Eburnean geodynamic evolution of the gold-rich southern Ashanti Belt, Ghana, with new field and geophysical evidence of pre-Tarkwaian deformations. Precambrian Research 204–205, 12-39.

Plümper, O., King, H.E., Vollmer, C., Ramasse, Q., Jung, H. and Austrheim, H. (2012) The legacy of crystal-plastic deformation in olivine: high-diffusivity pathways during serpentinization. Contributions to Mineralogy and Petrology 163, 701-724.

Putnis, A. (2009) Mineral Replacement Reactions. Reviews in Mineralogy and Geochemistry 70, 87-124.

Ramsay, J. and Huber, M. (1983) The Techniques of Modern Structural Geology, Vol. 1: Strain Analysis Academic Press, London.

Reddy, S., Timms, N., Pantleon, W. and Trimby, P. (2007) Quantitative characterization of plastic deformation of zircon and geological implications. Contributions to Mineralogy and Petrology 153, 625-645.

Reddy, S.M. and Hough, R.M. (2013) Microstructural evolution and trace element mobility in Witwatersrand pyrite. Contributions to Mineralogy and Petrology 166, 1269-1284.

Reddy, S.M., Timms, N.E., Trimby, P., Kinny, P.D., Buchan, C. and Blake, K. (2006) Crystal-plastic deformation of zircon: A defect in the assumption of chemical robustness. Geology 34, 257-260.

Reich, M., Kesler, S.E., Utsunomiya, S., Palenik, C.S., Chryssoulis, S.L. and Ewing, R.C. (2005) Solubility of gold in arsenian pyrite. Geochimica et Cosmochimica Acta 69, 2781-2796.

Ridley, J.R. and Diamond, L.W. (2000) Fluid chemistry of orogenic lode gold deposits and implications for genetic models, Gold in, pp. 141-162.

Ryan, C. (2000) Quantitative trace element imaging using PIXE and the nuclear microprobe. International Journal of Imaging Systems and Technology 11, 219-230.

Ryan, C., Kirkham, R., Hough, R., Moorhead, G., Siddons, D., De Jonge, M., Paterson, D., De Geronimo, G., Howard, D. and Cleverley, J. (2010a) Elemental X-ray imaging using the Maia detector array: The benefits and challenges of large solid-angle. Nuclear Instruments and Methods in Physics Research Section A: Accelerators, Spectrometers, Detectors and Associated Equipment 619, 37-43.

631 Ryan, C., Siddons, D., Kirkham, R., Dunn, P., Kuczewski, A., Moorhead, G., De Geronimo, G.,
632 Paterson, D., De Jonge, M. and Hough, R. (2010b) The new Maia detector system: methods for high
633 definition trace element imaging of natural material, X-Ray Optics and Microanalysis: Proceedings of
634 the 20th International Congress. AIP Publishing, pp. 9-17.
635 Ryan, C., Siddons, D., Kirkham, R., Li, Z., de Jonge, M., Paterson, D., Kuczewski, A., Howard, D.,
636 Dunn, P. and Falkenberg, G. (2014) MAIA X-ray fluorescence imaging: capturing detail in complex
637 natural samples, Journal of Physics: Conference Series. IOP Publishing, p. 012002.
638 Schwartz, M.O., Oberthür, T., Amanor, J. and Gyapong, W.A. (1992) Fluid inclusion re-equilibration
639 and P-T-X constraints on fluid evolution in the Ashanti gold deposit, Ghana. European Journal of
640 Mineralogy 4, 1017-1033.
641 Shannon, R.t. (1976) Revised effective ionic radii and systematic studies of interatomic distances in
642 halides and chalcogenides. Acta Crystallographica Section A: Crystal Physics, Diffraction, Theoretical
643 and General Crystallography 32, 751-767.
644 Shmulovich, K., Graham, C. and Yardley, B. (2001) Quartz, albite and diopside solubilities in H2O–
645 NaCl and H2O–CO2 fluids at 0.5–0.9 GPa. Contributions to Mineralogy and Petrology 141, 95-108.
646 Shvarov, Y.V. (2008) HCh: New potentialities for the thermodynamic simulation of geochemical
647 systems offered by Windows. Geochemistry International 46, 834-839.
648 Shvarov, Y.V. and Bastrakov, E. (1999) HCh: a software package for geochemical equilibrium
649 modelling. User's guide. Australian Geological Survey Organisation. Science and Resources, Record
650 25, 61.
651 Simmons, S.F. and Brown, K.L. (2007) The flux of gold and related metals through a volcanic arc,
652 Taupo Volcanic Zone, New Zealand. Geology 35, 1099-1102.
653 Sparks, H.A. and Mavrogenes, J.A. (2005) Sulfide melt inclusions as evidence for the existence of a
654 sulfide partial melt at Broken Hill, Australia. Economic Geology 100, 773-779.
655 Tian, Y., Etschmann, B., Liu, W., Borg, S., Mei, Y., Testemale, D., O'Neill, B., Rae, N., Sherman, D.M.
656 and Ngothai, Y. (2012) Speciation of nickel (II) chloride complexes in hydrothermal fluids: In situ XAS
657 study. Chemical Geology 334, 345-363.
658 Timms, N.E., Kinny, P.D., Reddy, S.M., Evans, K., Clark, C. and Healy, D. (2011) Relationship among
659 titanium, rare earth elements, U-Pb ages and deformation microstructures in zircon: Implications for
660 Ti-in-zircon thermometry. Chemical Geology 280, 33-46.
661 Tomkins, A.G. (2007) Three mechanisms of ore re-mobilisation during amphibolite facies
662 metamorphism at the Montauban Zn–Pb–Au–Ag deposit. Mineral. Deposita 42, 627-637.
663 Tomkins, A.G. and Mavrogenes, J.A. (2001) Redistribution of gold within arsenopyrite and löllingite
664 during pro-and retrograde metamorphism: application to timing of mineralization. Economic Geology
665 96, 525-534.

Tomkins, A.G. and Mavrogenes, J.A. (2002) Mobilization of gold as a polymetallic melt during pelite anatexis at the Challenger deposit, South Australia: a metamorphosed Archean gold deposit. Economic Geology 97, 1249-1271.

Tomkins, A.G., Pattison, D.R. and Frost, B.R. (2007) On the initiation of metamorphic sulfide anatexis. Journal of Petrology 48, 511-535.

Tomkins, A.G., Pattison, D.R. and Zaleski, E. (2004) The Hemlo gold deposit, Ontario: An example of melting and mobilization of a precious metal-sulfosalt assemblage during amphibolite facies metamorphism and deformation. Economic Geology 99, 1063-1084.

Tooth, B., Brugger, J., Ciobanu, C. and Liu, W. (2008) Modeling of gold scavenging by bismuth melts coexisting with hydrothermal fluids. Geology 36, 815-818.

Tooth, B., Ciobanu, C.L., Green, L., O'Neill, B. and Brugger, J. (2011) Bi-melt formation and gold scavenging from hydrothermal fluids: An experimental study. Geochimica et Cosmochimica Acta 75, 5423-5443.

Valley, J.W., Cavosie, A.J., Ushikubo, T., Reinhard, D.A., Lawrence, D.F., Larson, D.J., Clifton, P.H., Kelly, T.F., Wilde, S.A. and Moser, D.E. (2014) Hadean age for a post-magma-ocean zircon confirmed by atom-probe tomography. Nature Geoscience 7, 219-223.

Voudouris, P.C., Spry, P.G., Mavrogonatos, C., Sakellaris, G.-A., Bristol, S.K., Melfos, V. and Fornadel, A.P. (2013) Bismuthinite derivatives, lillianite homologues, and bismuth sulfotellurides as indicators of gold mineralization in the Stanos shear-zone related deposit, Chalkidiki, Northern Greece. The Canadian Mineralogist 51, 119-142.

Vukmanovic, Z., Reddy, S.M., Godel, B., Barnes, S.J., Fiorentini, M.L., Barnes, S.-J. and Kilburn, M.R. (2014) Relationship between microstructures and grain-scale trace element distribution in komatiite-hosted magmatic sulphide ores. Lithos 184, 42-61.

Xia, F., Brugger, J., Chen, G., Ngothai, Y., O'Neill, B., Putnis, A. and Pring, A. (2009) Mechanism and kinetics of pseudomorphic mineral replacement reactions: a case study of the replacement of pentlandite by violarite. Geochimica et Cosmochimica Acta 73, 1945-1969.

Yao, Y. and Robb, L.J. (2000) Gold mineralization in Palaeoproterozoic granitoids at Obuasi, Ashanti region, Ghana: Ore geology, geochemistry and fluid characteristics. South African Journal of Geology 103, 255-278.

Zhao, J., Brugger, J., Grundler, P.V., Xia, F., Chen, G. and Pring, A. (2009) Mechanism and kinetics of a mineral transformation under hydrothermal conditions: Calaverite to metallic gold. American Mineralogist 94, 1541-1555.

**Figure list:**

Figure 1: (A) Geology of northern Ghana Paleoproterozoic basement (simplified from Allibone et al., 2002). The Obuasi giant deposit is located in the Kumasi Group metasedimentary rocks close to the contact with the Sefwi Group volcanic greenstones of the Ashanti belt. (B) Typical mineralised and laminated quartz vein, containing wall rock fragments, from Obuasi underground drive, level 30#1 Crosscut 318; (C) Microphotograph of the sediment sample DF038 (phyllites). Gold-bearing arsenopyrites are surrounded by quartz strain shadows parallel with $S2_{Ob}$ and refolded by $S3_{Ob}$; (D) BSE image of mineralised quartz vein sample DF091b, native gold precipitated along muscovite cleavage planes and developed in fractures crosscutting the quartz veins. The dominant fracture is parallel with the hinge line of $S3_{Ob}$ crenulation cleavage; (E) Textures in gold-bearing arsenopyrites (BSE sample 318-15). The arsenopyrite grains are euhedral and native gold is present in microfractures and grain boundary regions. $Apy_{(II)}$ has a higher atomic mass; (F) Fracture in quartz vein filled with gold and accessory sulfides (sample DF099 - BSE image).

Figure 2: Backscattered electron images showing internal arsenopyrite textures. (A) to (C) the $Apy_{(I)}$ grains are cut by $Apy_{(II)}$. $Apy_{(II)}$ has a brighter BSE response indicating higher average atomic mass (in this case enriched in arsenic); (D) late generation $Py_{(III)}$ postdating the arsenopyrites; (E) and (F) Arsenopyrite aggregates studied in further details in figures 3, 4 and 5. Native gold is present in microfractures in Apy or at grain boundaries.

Figure 3: Sample 215-7b arsenopyrite aggregate. (A) Synchrotron XFM RGB image (Red, Calcium; Green, Iron; Blue, Arsenic). The aggregate is composed of arsenopyrites with interstitial pyrites and ankerite. The matrix is composed of muscovite, chlorite and quartz; (B) Synchrotron XFM RGB image (yellow, Au; blue, Ni). The sulphides are gold-bearing arsenopyrites ($Apy_{(I)}$) and Ni-enriched pyrites ($Py_{(III)}$). In $Apy_{(I)}$, the gold content is zoned with high concentrations in epitaxial overgrowth regions, whereas the cores are gold-poor. Ni is enriched in both the interstitial $Py_{(III)}$ and the $Apy_{(II)}$ rims, parallel with microfractures and grain boundaries. The grain boundaries and $Apy_{(II)}$ are contoured in red. (C) to (H) NanoSIMS elemental maps of Apy zones indicated on (B). (C) and (F) $^{60}Ni^{32}S$ distribution; (D and (G) $^{197}Au$ distribution; (E) and (H) composite RGB image (yellow, $^{197}Au$; blue $^{60}Ni^{32}S$). $Apy_{(II)}$ rims are gold-poor and Ni enriched. They cut across the fine, micron scale gold-rich oscillatory zoning of $Apy_{(I)}$, with sharp irregular boundaries. Native gold particles are located in a healed microfracture.

Figure 4: Arsenopyrite in crenulated phyllites (sample 215-20). (A) Backscattered electron image, the grain boundaries of $Apy_{(I)}$, $Apy_{(II)}$ and $Py_{(III)}$ are contoured in red. Position of figures (C), (D) and (E) are indicated; (B) Coloured EBSD map showing crystallographic misorientations in the range 0-10° of arsenopyrite and pyrite. Subgrains developed in the arsenopyrite are marked in black. The pyrite

remains undeformed. There is no change in crystallographic orientation where $Apy_{(I)}$ changes to $Apy_{(II)}$; including preservation of the zones of crystal-plastic deformation. (C) NanoSIMS map of $^{60}Ni^{32}S$ showing Ni distribution; (D) NanoSIMS map of $^{197}Au$; (E) NanoSIMS composite RGB image (yellow, $^{197}Au$; blue $^{60}Ni^{32}S$). The $Apy_{(II)}$ is gold-poor and crosscuts the fine, micron scale gold-rich oscillatory zonation of the arsenopyrites. Ni-bearing $Py_{(III)}$ is located in the healed microfracture and the width of $Apy_{(II)}$ is up to 3 times greater in the areas associated with high densities of misorientation observed on (B).

Figure 5: Sample 215-7b arsenopyrite aggregate 2. (A) Synchrotron XFM RGB image (Red, Calcium; Green, Iron; Blue, Arsenic). The aggregate is composed of arsenopyrites with interstitial pyrites and ankerite. The matrix is composed of muscovite, chlorites, ankerites and quartz; (B) Synchrotron XFM RGB image (yellow, Au; blue, Ni). The sulphides are gold-bearing arsenopyrites ($Apy_{(I)}$), with small replacement zones of nickeliferous arsenopyrite ($Apy_{(II)}$) and Ni-enriched pyrites ($Py_{(III)}$). In $Apy_{(I)}$, the gold concentration is zoned with higher concentration in epitaxial overgrowth whereas the cores are gold-poor. The grain boundaries and $Apy_{(II)}$ are contoured in red. Position of NanoSIMS elemental maps are indicated (Fig. 6); (C) Au and Ni concentrations along the A-A' traverse. In the microfracture labelled in (A), the high Au and Ni values reflect the presence of native Au and $Py_{(III)}$. The Au concentration is below detection limit in the $Apy_{(II)}$ while the Ni distribution show an edge of high concentration near the sharp contact with $Apy_{(I)}$. In $Apy_{(I)}$, Au concentrations attain 2000 ppm, whereas the Ni concentrations decrease from approximately 750 ppm to below detection limit toward the centre of the grain.

Figure 6: NanoSIMS elemental maps of Apy zones indicated on figure 4. (A) and (B) composite RGB image (yellow, $^{197}Au$; blue $^{60}Ni^{32}S$). The $Apy_{(II)}$ is gold-poor and cuts across the fine, micron scale gold-rich oscillatory zoning of $Apy_{(I)}$. Native gold particles are located in a healed microfracture.

Figure 7: pH-Eh activity diagram for the predominant Au (A) and Ni (B) speciation at 350 ºC, 2k bar. The solution contains $Cl^-$ ($\alpha$=0.065), $SO_4^{2-}$ ($\alpha$=0.03), $Fe^{2+}$ ($\alpha$=0.01), and 1ppb-10ppm amount of $Au^+$ or $Ni^{2+}$. The dashed blue lines show the boundary of different sulfur species, the dashed green lines show the field of Fe minerals as redox buffer. The solid red line and yellow line indicate the boundary of the predominant Au or Ni species (with 1 ppb to 10 ppm Au or Ni in the solution the thick, red to yellow dash lines). The pentlandite stability field represents the domain that Ni is predominantly stable as a solid sulphide mineral phase (arsenopyrite in our case study).

Figure 8: Impact of the addition of sulphur to the fluid by changing $\log fS_2(g)$ from -15 to -6 at 350 ºC, 2k bar (e.g. as the arsenopyrite replacement reaction occurs sulphur is released). The initial reactant contains 1 kg $H_2O$, 1 molal $Cl^-$, $10^{-4}$ molal $Ni^{2+}$, $10^{-3}$ molal $Fe^{2+}$, 1 g native gold, 1 g arsenopyrite and

some $Na^+$ to balance the charge. The pH is fixed at 7 and the initial log$fO_2$ of -33 is chosen for the reaction. (A) The total amount of Ni and Au in the solution. (B) The stable mineral phases as the reaction proceeds.

Figure 9: Reaction removing $CO_2$ from the fluid as carbonate precipitates. Temperature of 350 ºC, 2k bar containing 1 kg $H_2O$, 1 molal $H_2S$(aq), 1 molal $Cl^-$, $10^{-4}$ molal $Ni^{2+}$, $10^{-3}$ molal $Fe^{2+}$, 1 g native gold, 10 g quartz, 1 g calcite and some $Na^+$ to balance the charge. The pH changes from 5.7 to 8 as the reaction proceeds, and log$fO_2$ changes from -28.9 to -30, depending on the amount of $CO_2$ in the system. (A) The total amount of Au and Si dissolved in solution as $CO_2$ is removed from the fluids; (B) Change of pH and oxygen fugacity during reaction; (C) Concentration of important sulfur speciation and the total sulfur concentration in the fluids.

Figure 10: Interpretation of arsenopyrite alteration, metal remobilisation and native gold precipitation in fracture networks and quartz vein fold hinges. (A) The arsenopyrite-hosted mineralisation is equally distributed along the strike of the veins. The highest gold grades and native gold are hosted in the $F3_{Ob}$ fold hinges of the quartz vein. (B) Partial crystal-plastic recrystallisation of the arsenopyrites was synchronous with $D3_{Ob}$ (Fougerouse et al. in press). This microstructure and intragranular microfractures allowed fluid infiltration and psuedomorphic replacement of Au-rich Apy with Ni-bearing but Au-barren Apy. Psuedomorphic replacement also occurred on undeformed boundaries of the grains. Ni-enriched pyrite crystallised synchronously in intragranular microfractures; (C) Low volume Ni-bearing fluid migrated pervasively in the wall rock, along the $S3_{Ob}$ cleavage planes, grain boundaries and microfracture networks, facilitating reaction and leading to release of gold and S into the fluid; (D) Native gold precipitates in fracture networks in the previously formed quartz veins, as well as microcrack networks in the wall rock to a lesser extent.

**Table list:**

Table 1: Electron microprobe analysis of different domains of Apy in Wt%. BDL refers to “Below Detection Limit” (230 ppm). Modified from Fougerouse et al. (in press).

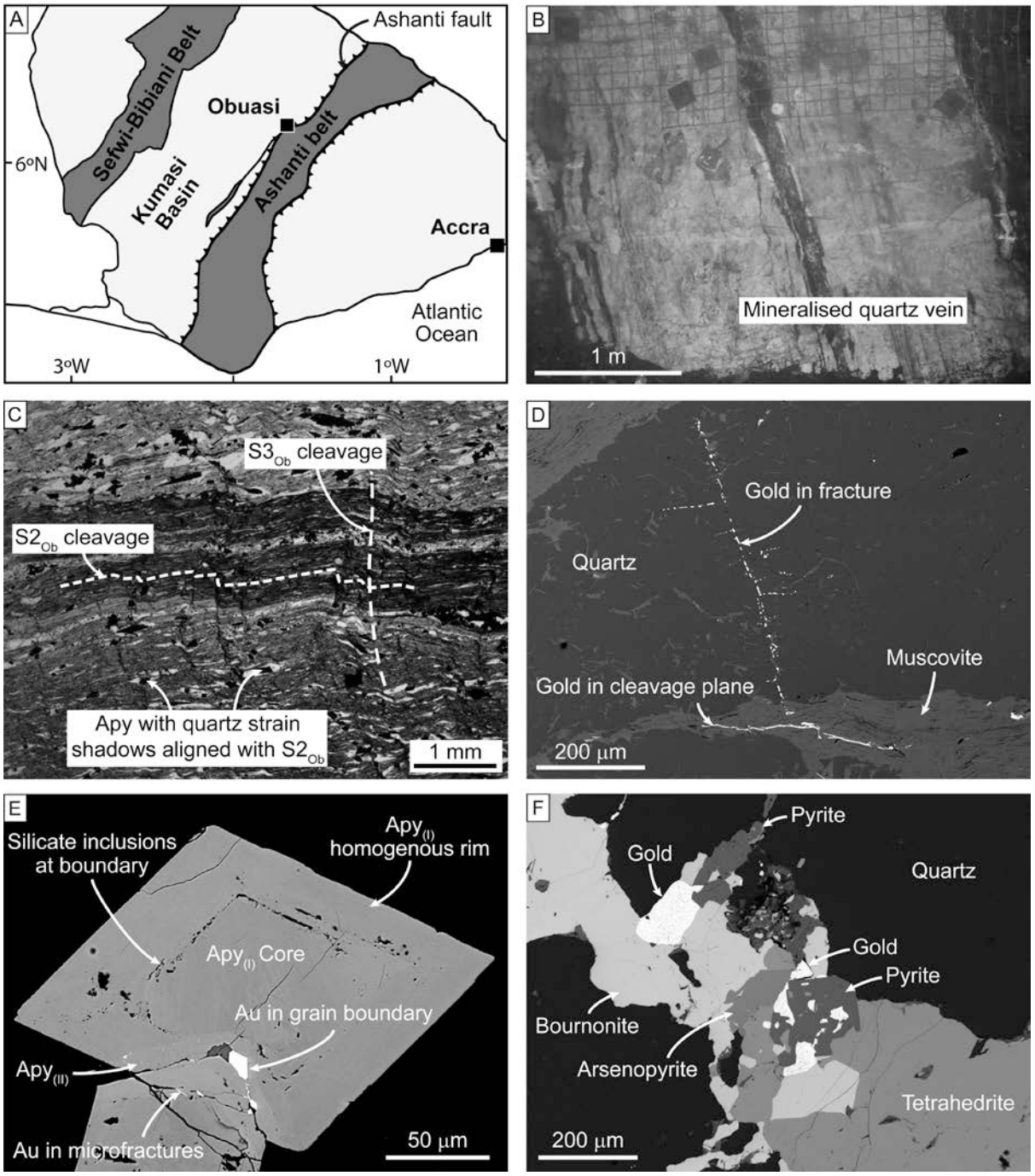
A
Ashanti fault
Sefwi-Bibiani Belt
Obuasi
6°N
Kumasi Basin
Ashanti belt
Accra
Atlantic Ocean
3°W
1°W
B
Mineralised quartz vein
1 m
C
S3Ob cleavage
S2Ob cleavage
Apy with quartz strain shadows aligned with S2Ob
1 mm
D
Gold in fracture
Quartz
Muscovite
Gold in cleavage plane
200 μm
E
Silicate inclusions at boundary
Apy(I) homogenous rim
Apy(I) Core
Au in grain boundary
Apy(II)
Au in microfractures
50 μm
F
Pyrite
Gold
Quartz
Gold
Pyrite
Bournonite
Arsenopyrite
Tetrahedrite
200 μm

801

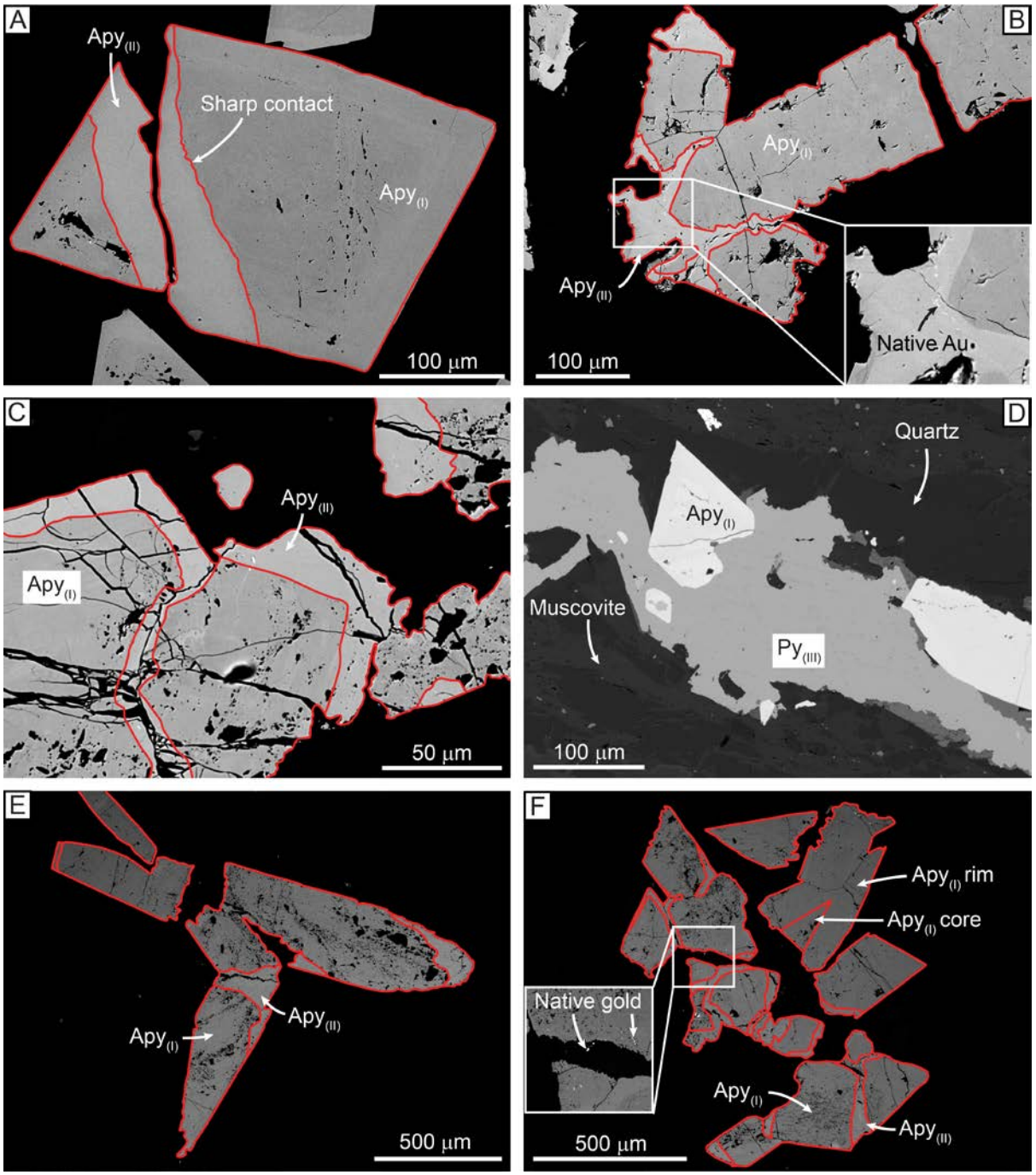
A
Apy(II)
Sharp contact
Apy(I)
100 µm
B
Apy(I)
Apy(II)
Native Au
100 µm
C
Apy(II)
Apy(I)
50 µm
D
Quartz
Apy(I)
Muscovite
Py(III)
100 µm
E
Apy(I)
Apy(II)
500 µm
F
Apy(I) rim
Apy(I) core
Native gold
Apy(I)
Apy(II)
500 µm

802

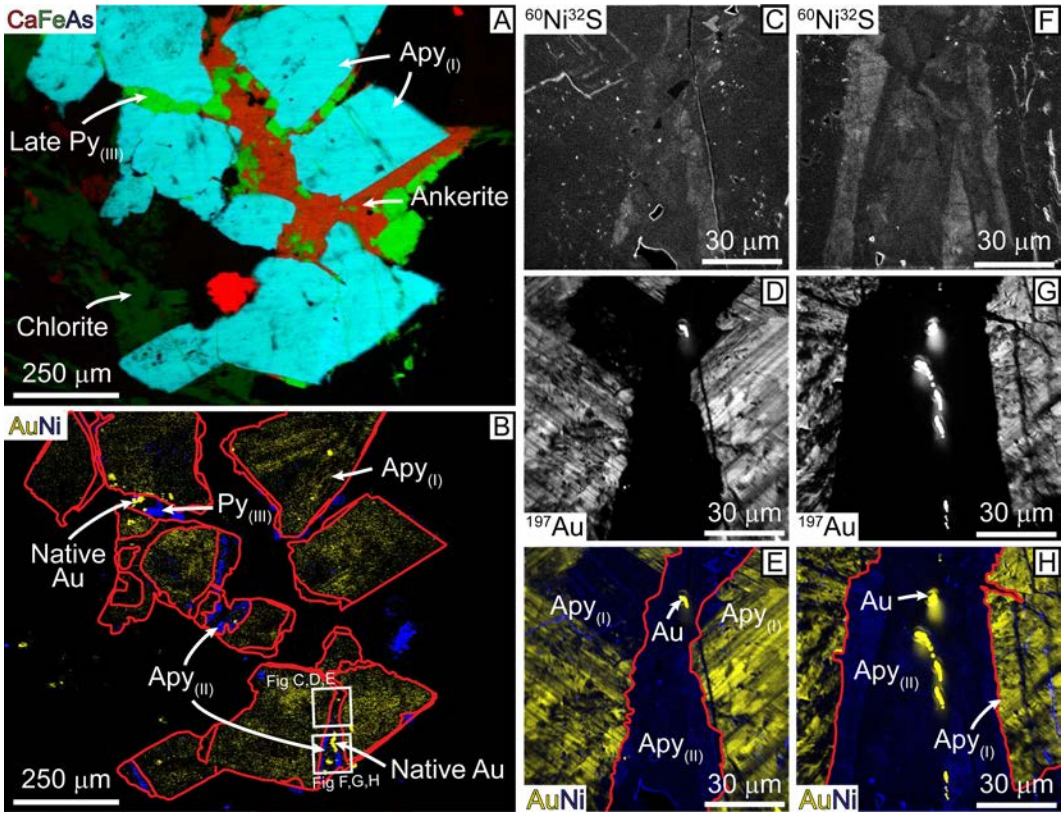
CaFeAs
A
Apy(I)
Late Py(III)
Ankerite
Chlorite
250 µm
AuNi
B
Apy(I)
Py(III)
Native Au
Apy(II)
Fig C,D,E
Fig F,G,H
Native Au
250 µm
60Ni32S
C
30 µm
60Ni32S
F
30 µm
D
30 µm
G
197Au
30 µm
197Au
30 µm
E
Apy(I)
Au
Apy(I)
Apy(II)
AuNi
30 µm
H
Au
Apy(II)
Apy(I)
AuNi
30 µm

803

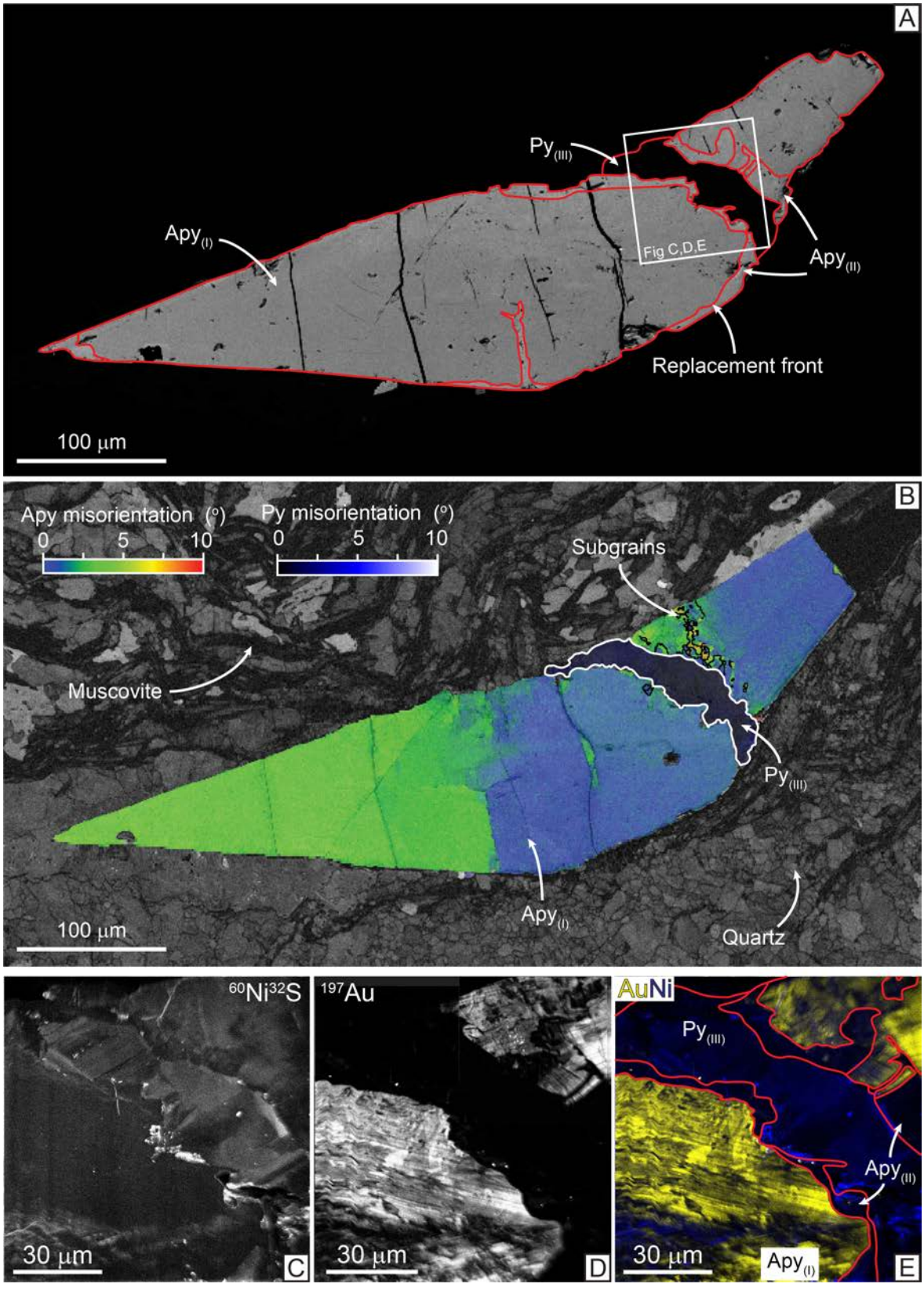
A
Py(III)
Apy(I)
Fig C,D,E
Apy(II)
Replacement front
100 μm
B
Apy misorientation (°)
0 5 10
Py misorientation (°)
0 5 10
Subgrains
Muscovite
Py(III)
Apy(I)
Quartz
100 μm
60Ni32S
30 μm
C
197Au
30 μm
D
AuNi
Py(III)
Apy(II)
30 μm
Apy(I)
E

804

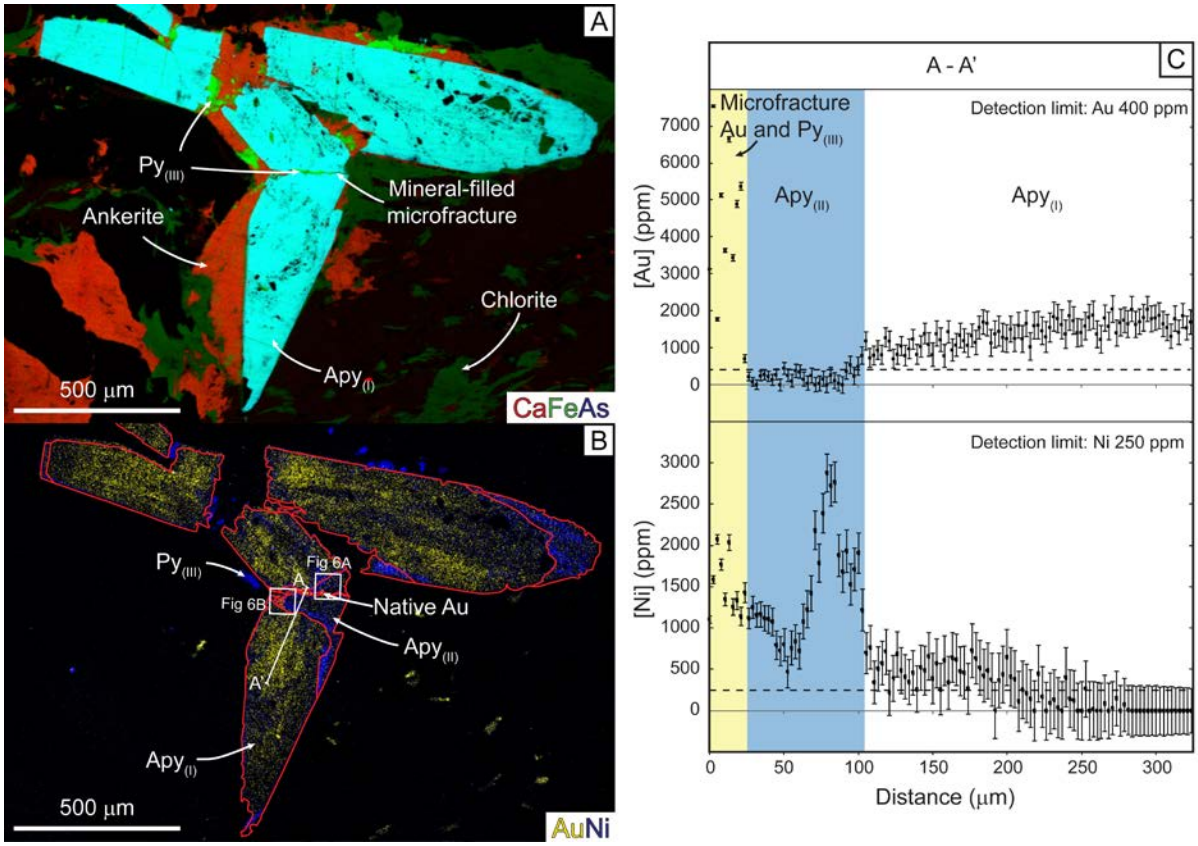
A
Py(III)
Mineral-filled microfracture
Ankerite
Chlorite
Apy(I)
500 µm
CaFeAs
B
Py(III)
Fig 6A
A
Fig 6B
Native Au
Apy(II)
A'
Apy(I)
500 µm
AuNi
C
A - A'
Microfracture Au and Py(III)
Apy(II)
Apy(I)
Detection limit: Au 400 ppm
[Au] (ppm)
Detection limit: Ni 250 ppm
[Ni] (ppm)
Distance (µm)

805

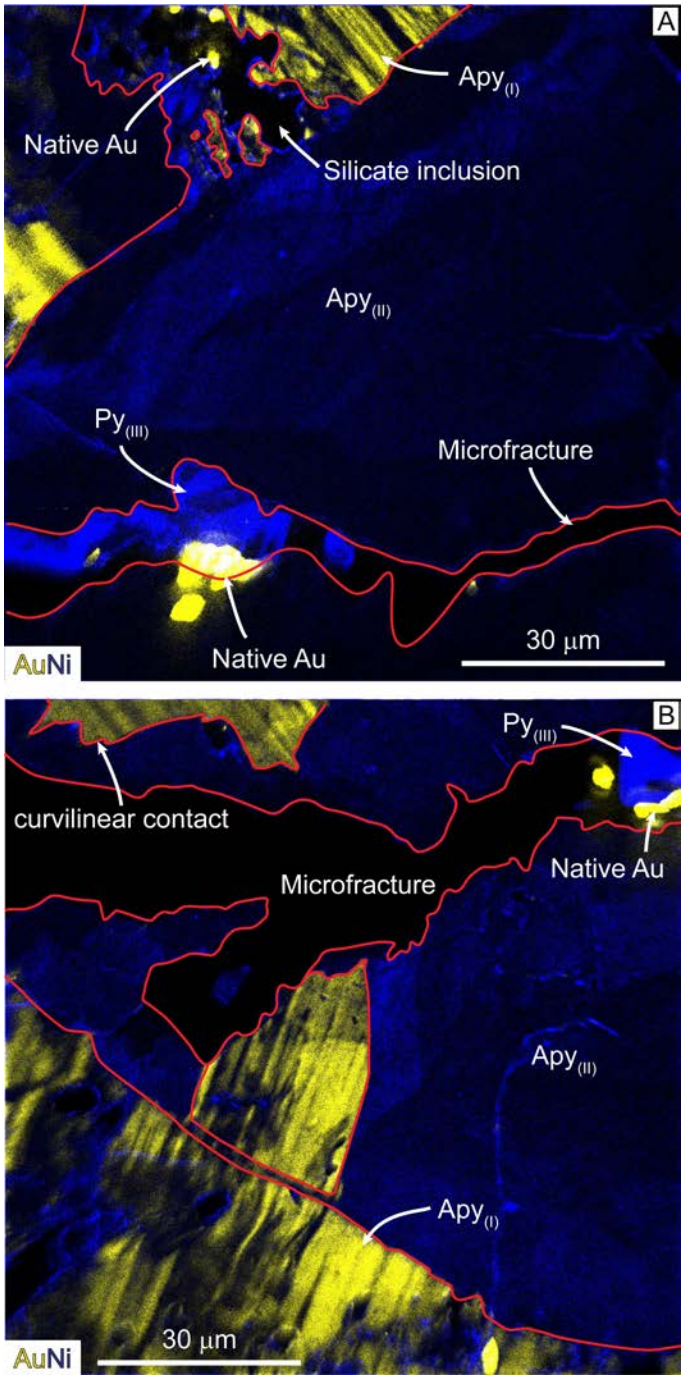
A
Native Au
Apy(I)
Silicate inclusion
Apy(II)
Py(III)
Microfracture
Native Au
30 μm
AuNi
B
Py(III)
curvilinear contact
Native Au
Microfracture
Apy(II)
Apy(I)
30 μm
AuNi

806

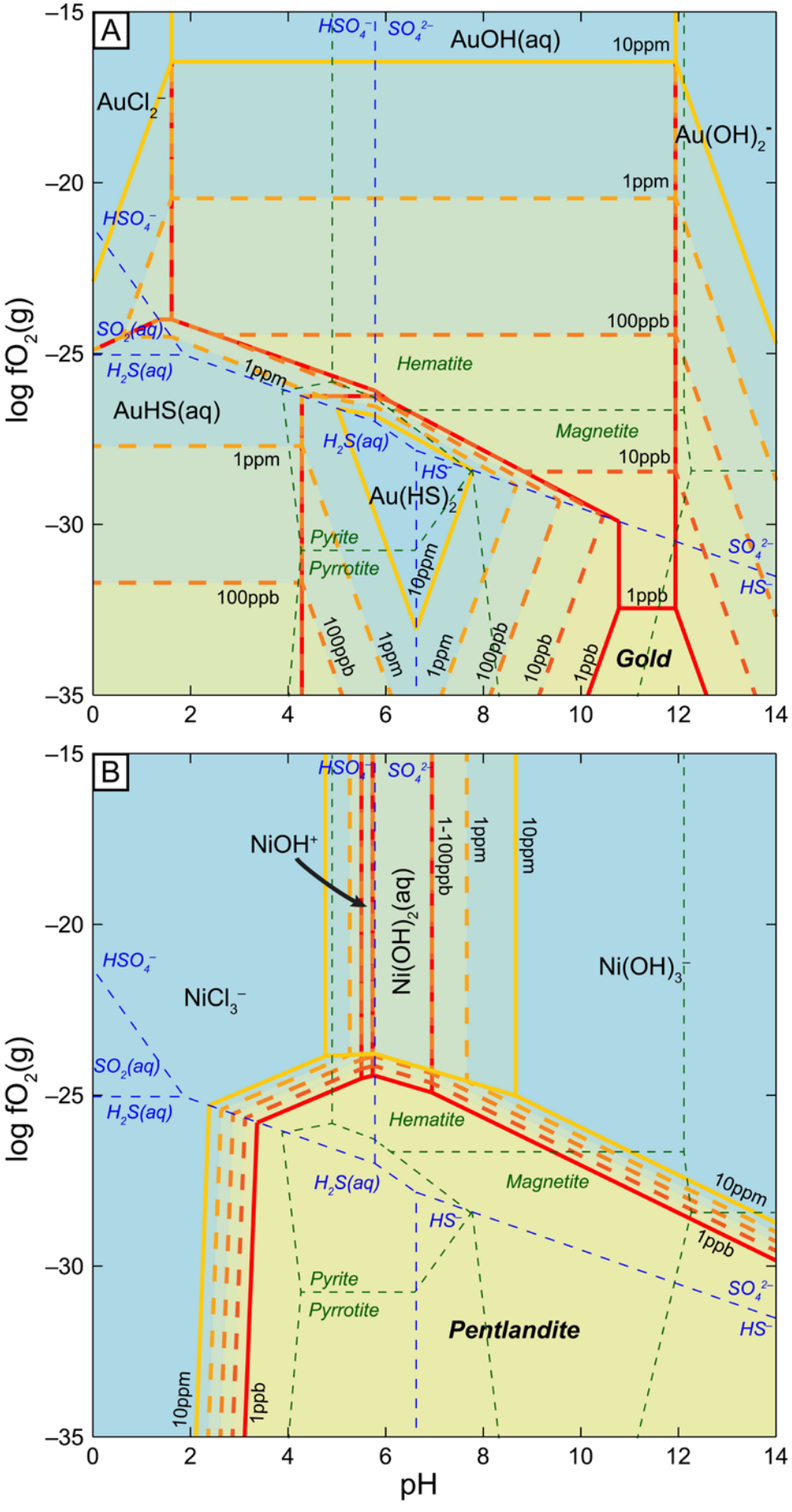
A
B
log fO2(g)
pH
HSO4−
SO4 2−
AuOH(aq)
AuCl2−
Au(OH)2−
AuHS(aq)
Au(HS)2
H2S(aq)
SO2(aq)
HS−
Hematite
Magnetite
Pyrite
Pyrrotite
Gold
Pentlandite
NiOH+
Ni(OH)2(aq)
NiCl3−
Ni(OH)3−
10ppm
1ppm
100ppb
1ppb
1-100ppb

807

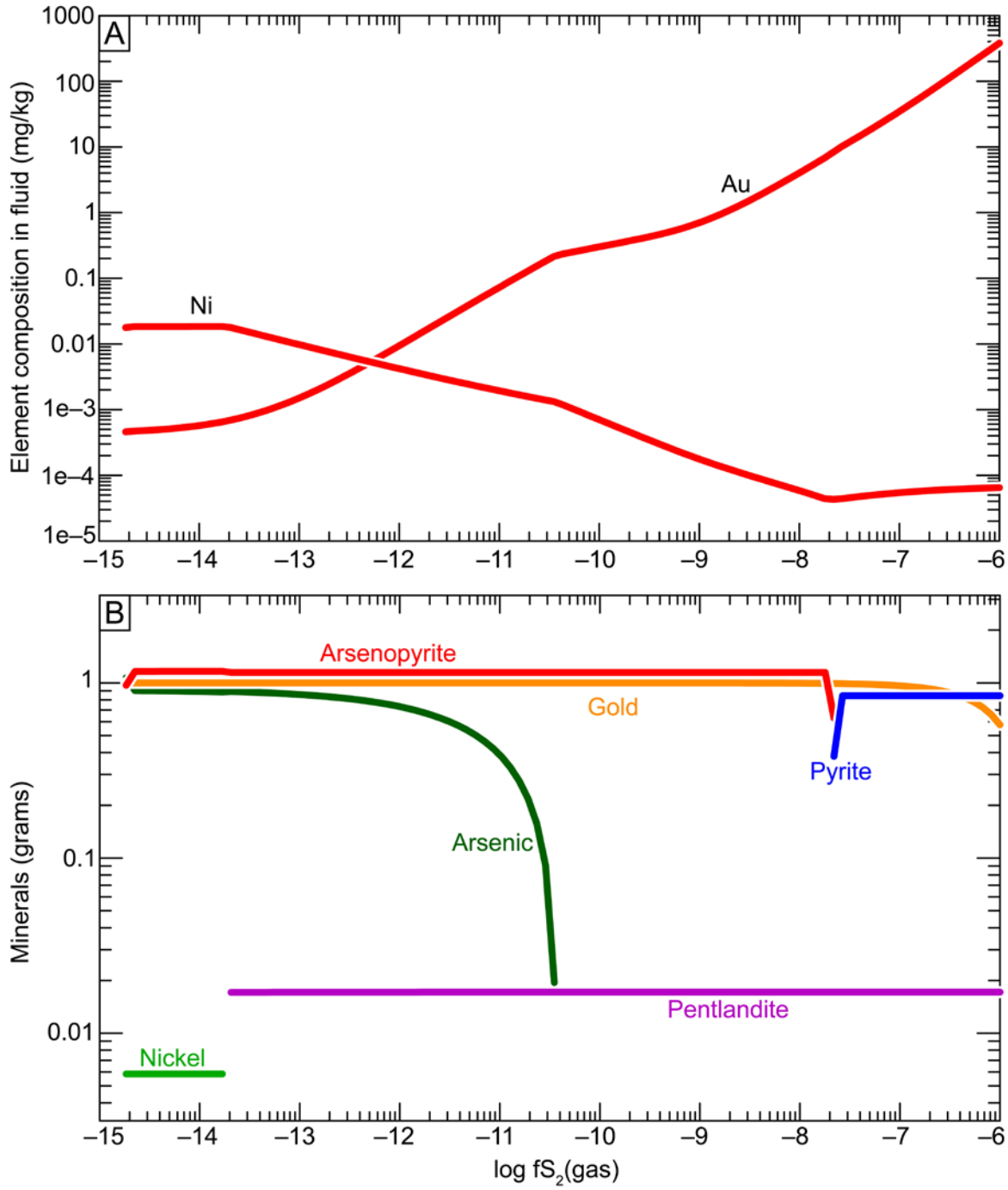
A
Element composition in fluid (mg/kg)
1000
100
10
1
0.1
0.01
1e–3
1e–4
1e–5
Au
Ni
–15
–14
–13
–12
–11
–10
–9
–8
–7
–6
B
Minerals (grams)
1
0.1
0.01
Arsenopyrite
Gold
Pyrite
Arsenic
Pentlandite
Nickel
log fS2(gas)

808

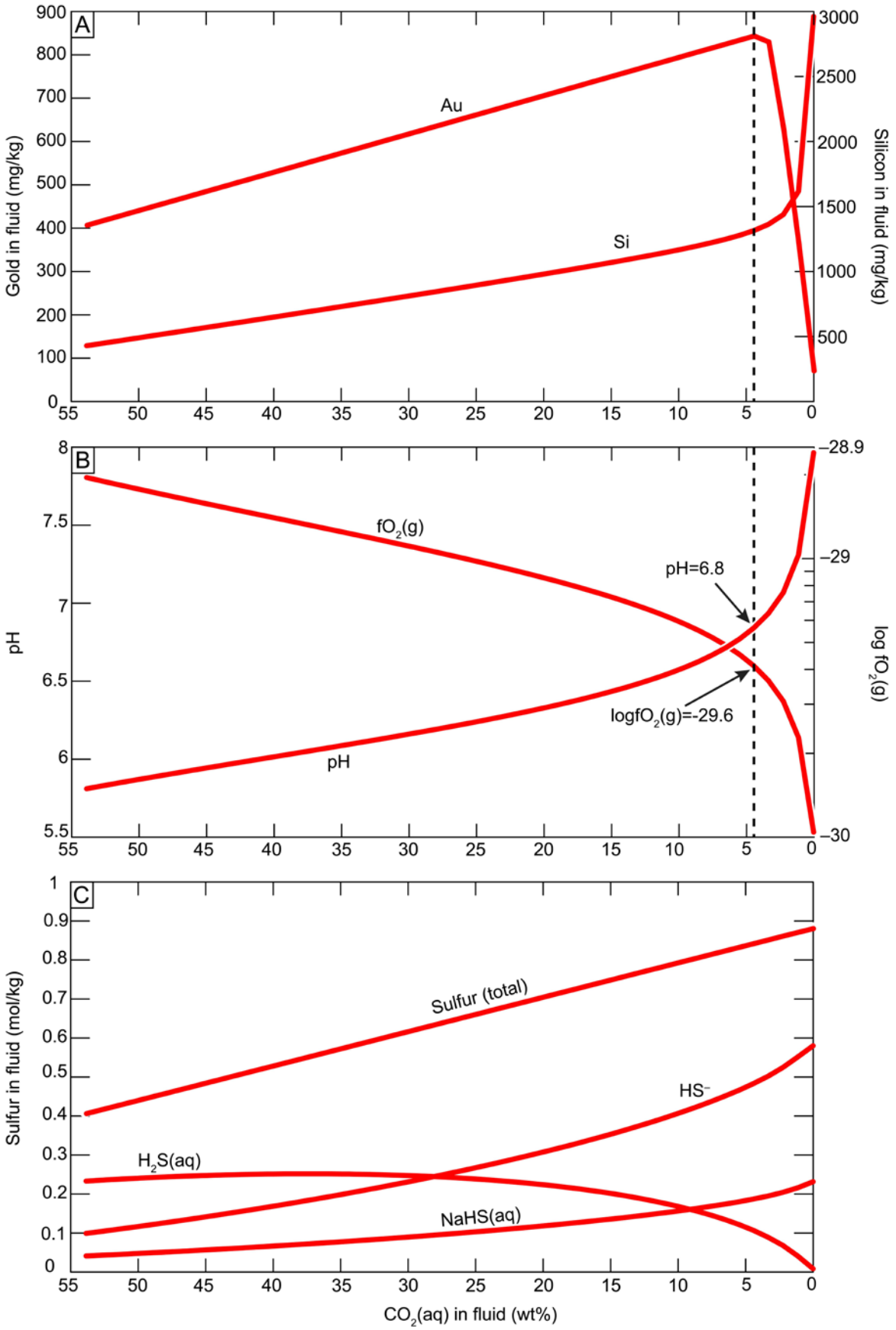
A
Gold in fluid (mg/kg)
Silicon in fluid (mg/kg)
Au
Si
B
pH
log fO2(g)
fO2(g)
pH=6.8
logfO2(g)=-29.6
pH
C
Sulfur in fluid (mol/kg)
Sulfur (total)
HS⁻
H2S(aq)
NaHS(aq)
CO2(aq) in fluid (wt%)

809

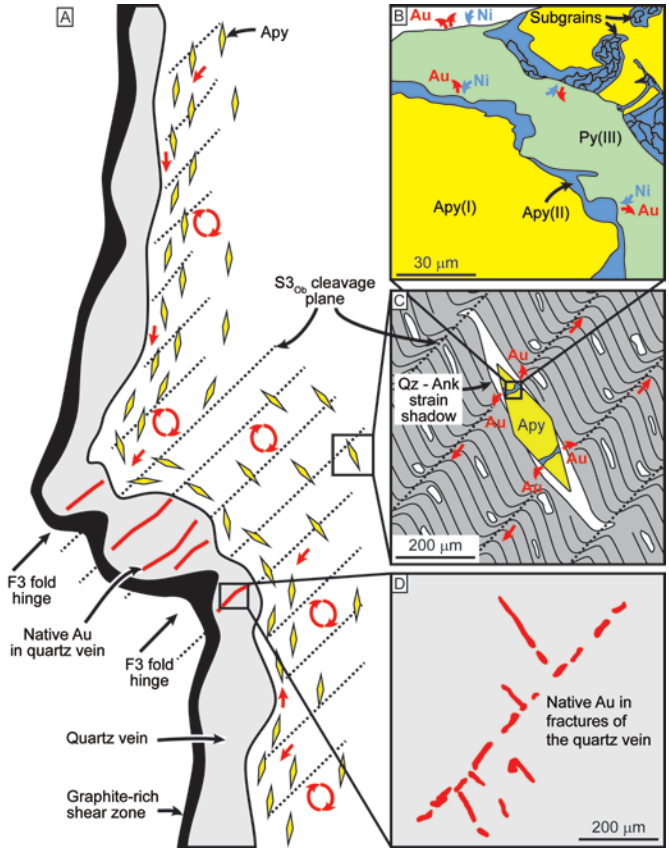
A
Apy
B
Au
Ni
Subgrains
Au
Ni
Py(III)
Apy(I)
Apy(II)
Ni
Au
30 μm
S3Oe cleavage plane
C
Qz - Ank strain shadow
Au
Au
Apy
Au
Au
200 μm
F3 fold hinge
Native Au in quartz vein
F3 fold hinge
D
Native Au in fractures of the quartz vein
Quartz vein
Graphite-rich shear zone
200 μm

810